BIROn - Birkbeck Institutional Research Online

Rai, A. and Liu, T. and Glauser, S. and Katrukha, E.A. and Estévez-Gallego, J. and Rodríguez-García, R. and Fang, W.-S. and Díaz, J.F. and Steinmetz, M.O. and Altman, K.-H. and Kapitein, L.C. and Moores, Carolyn and Akhmanova, A. (2019) Taxanes convert regions of perturbed microtubule growth into rescue sites. Nature Materials , ISSN 1476-1122. (In Press)

Downloaded from: http://eprints.bbk.ac.uk/29944/

Usage Guidelines:
Please refer to usage guidelines at http://eprints.bbk.ac.uk/policies.html or alternatively contact lib-eprints@bbk.ac.uk.

2. Supplementary Information:

A. Flat Files

Item	Present?	Filename This should be the name the file is saved as when it is uploaded to our system, and should include the file extension. The extension must be .pdf	A brief, numerical description of file contents. i.e.: *Supplementary Figures 1-4, Supplementary Discussion, and Supplementary Tables 1-4.*
Supplementary Information	Yes	Rai_Supplementary File as per guideline_20092019_eve.pdf	The file contains Supplementary Figures 1-7, Supplementary Figure 1-7 legends and Supplementary Video 1 and 2 legends.
Reporting Summary	Yes	RAI_nr-reporting-summary 20092019.pdf	

B. Additional Supplementary Files

Type	Number If there are multiple files of the same type this should be the numerical indicator. i.e. "1" for Video 1, "2" for Video 2, etc.	Filename This should be the name the file is saved as when it is uploaded to our system, and should include the file extension. i.e.: *Smith_ Supplementary_Video_1.mov*	Legend or Descriptive Caption Describe the contents of the file
Supplementary Video	1	Rai_Supplementary Video-1.avi	**Fchitax-3 accumulation at the growing microtubule plus end.** The movie illustrates formation of an Fchitax-3 accumulation close to the growing microtubule plus end, as depicted in Fig. 2a. The experiment was performed in the presence of tubulin (15 μM), mCherry-EB3 (20 nM) and

			Fchitax-3 (100 nM). The movie consists of 177 frames acquired with a 2s interval between frames and an exposure time of 100ms. Scale bar, 2µm. The movie is representative of more than 5 independent experiments.
Supplementary Video	2	Rai_Supplementary Video-2.avi	**Laser severing experiment showing Fchitax-3 accumulation zone stabilizes microtubule lattice.** The movie starts just after ablating the Fchitax-3 accumulation area with a 532nm laser as shown in Fig. 2h. After ablation of the growing microtubule at Fchitax-3 accumulation, both the newly generated ends survived and started growing again. The experiment was performed in the presence of tubulin (15µM, supplemented with 3% rhodamine-tubulin), mCherry-EB3 (20nM) and Fchitax-3 (100nM). The movie consists of 750 frames acquired in a stream acquisition mode with an exposure time of 100ms. Scale bar, 2µm. The movie is representative of 5 independent experiments.
NMR Data	1	Rai_Supplementary_Fig.3b_SourceData_1HNMR.zip	1H-NMR
NMR Data	2	Rai_Supplementary_Fig.3b_SourceData_C13NMR.zip	C13-NMR
Supplementary Data	1	Rai_Supplementary_Fig.1_SourceData.xlsx	An Excel sheet with the numerical data on the quantification of occurrence of stable rescue sites, intensity

			measurement of single molecules of Fchitax-3, photobleaching time traces and intensity measurement of Fchitax-3 at stable rescue sites.
Supplementary Data	2	Rai_Supplementary_Fig.2_SourceData.xlsx	An Excel sheet with the numerical data on the analysis of the time intervals between the appearances of two consecutive accumulations, analysis of duration, length and frequency of Fchitax-3 accumulations at plus and minus ends of microtubules and quantification of microtubule growth rates.
Supplementary Data	3	Rai_Supplementary_Fig.4_SourceData.xlsx	An Excel sheet with the numerical data on the quantification of microtubule growth rates, catastrophe frequencies and accumulation frequencies, accumulation length and intensity profiles showing the reduction in the EB3 signal.
Supplementary Data	4	Rai_Supplementary_Fig.5_SourceData.xlsx	An Excel sheet with the numerical data on the quantification of characteristic photobleaching traces, decay times, comparison of the best fits for the models, dependence of initial values and tubulin states, kinetics of tubulin states, numerically solved FRAP curves and fluorescence intensities.
Supplementary Data	5	Rai_Supplementary_Fig.6_SourceData.xlsx	An Excel sheet with the numerical data on the fiber diffraction analysis of microtubules during different assembly conditions in the

			presence of Taxol.
Supplementary Data	6	Rai_Supplementary_Fig.7_SourceData.xlsx	An Excel sheet with the numerical data on the quantification of CAMSAP3 binding near Fchitax-3 accumulations, fluorescence intensity profiles for fluorescence recovery after photobleaching and distribution of the Fchitax-3 accumulations.

3. Source Data

Parent Figure or Table	Filename This should be the name the file is saved as when it is uploaded to our system, and should include the file extension. i.e.: *Smith_SourceData_Fig1.xls,* or *Smith_Unmodified_Gels_Fig1.pdf*	Data description e.g.: Unprocessed Western Blots and/or gels, Statistical Source Data, etc.
Source Data Fig. 1	Rai_Fig.1_SourceData.xlsx	An Excel sheet with the numerical data on the quantification of Fchitax-3 and Flutax-2 intensity on GDP lattice and on stable rescue sites and frequency of the occurrence of stable rescue sites in vitro and in cells.
Source Data Fig. 2	Rai_Fig.2_SourceData.xlsx	An Excel sheet with the numerical data on the quantification of fluctuations of EB3 fluorescence intensities, microtubule growth rates and microtubule survival after the ablation.
Source Data Fig. 3	Rai_Fig.3_SourceData.xlsx	An Excel sheet with the numerical data on the quantification of Fchitax-3 accumulation frequencies and time plots of the normalized maximum intensity of fitted EB3 comets and the normalized area under the curve (AUC) of fitted Fchitax-3 intensities.

Source Data Fig. 4	Rai_Fig.4_SourceData.xlsx	An Excel sheet with the numerical data for the intensity time traces of Fchitax-3, best fits to a single profile using Michaelis-Menten or the autocatalysis model, analysis of rate constants, intensity time traces for the FRAP analysis of Fchitax-3 accumulation and modeling of FRAP curves.
Source Data Fig. 5	Rai_Fig.5_SourceData.xlsx	An Excel sheet with the numerical data for Fchitax-3 fluorescence intensity profiles and quantifications of the normalized value of fluorescence intensities in different conditions and the rate constant of photobleaching.
Source Data Fig. 6	Rai_Fig.6_SourceData.xlsx	An Excel sheet with the numerical data on the quantification of cryo-EM defect analysis, transverse microtubule tip fluctuations, fluorescence intensity profiles and quantifications showing CAMSAP3 intensity, fluorescence intensity profiles and quantification of tubulin recovery after FRAP and quantification of EB3 fluorescence.

Taxanes convert regions of perturbed microtubule growth into rescue sites

Ankit Rai[1], Tianyang Liu[2], Simon Glauser[3], Eugene A. Katrukha[1], Juan Estévez-Gallego[4], Ruddi Rodríguez-García[1], Wei-Shuo Fang[5], J. Fernando Díaz[4], Michel O. Steinmetz[6,7], Karl-Heinz Altmann[3], Lukas C. Kapitein[1], Carolyn A. Moores[2] and Anna Akhmanova[1]

[1] Cell Biology, Neurobiology and Biophysics, Department of Biology, Faculty of Science, Utrecht University, Padualaan 8, 3584 CH Utrecht, the Netherlands

[2] Institute of Structural and Molecular Biology, Birkbeck, University of London, Malet Street, London, United Kingdom

[3] Department of Chemistry and Applied Biosciences, Institute of Pharmaceutical Sciences, ETH Zürich, 8092 Zürich, Switzerland

[4] Chemical and Physical Biology, Centro de Investigaciones Biológicas, Consejo Superior de Investigaciones Científicas CIB-CSIC, Ramiro de Maeztu 9, 28040, Madrid, Spain

[5] State Key Laboratory of Bioactive Substances and Functions of Natural Medicines, Institute of Materia Medica, CAMS & PUMC, 2A Nan Wei Road, Beijing, 100050, China

[6] Laboratory of Biomolecular Research, Division of Biology and Chemistry, Paul Scherrer Institut, 5232 Villigen PSI

[7] University of Basel, Biozentrum, CH-4056 Basel, Switzerland

Corresponding author: Anna Akhmanova, a.akhmanova@uu.nl; ORCID 000-0002-9048-8614.

Abstract

Microtubules are polymers of tubulin dimers, and conformational transitions in the microtubule lattice drive microtubule dynamic instability and affect various aspects of microtubule function. The exact nature of these transitions and their modulation by anti-cancer drugs such as Taxol and epothilone, which can stabilize microtubules but also perturb their growth, are poorly understood. Here, we directly visualize the action of fluorescent Taxol and epothilone derivatives and show that microtubules can transition to a state that triggers cooperative drug binding to form regions with altered lattice conformation. Such regions emerge at growing microtubule ends that are in a pre-catastrophe state and inhibit microtubule growth and shortening. Electron microscopy and in vitro dynamics data indicate that taxane accumulation zones represent incomplete tubes that can persist, incorporate tubulin dimers and repeatedly induce microtubule rescues. Thus, taxanes modulate the material properties of microtubules by converting destabilized growing microtubule ends into regions resistant to depolymerization.

48 Microtubules are cytoskeletal filaments essential for numerous cellular functions. They are
49 formed by the polymerization of tubulin dimers into a regular lattice[1]. Microtubule lattices
50 display structural plasticity, which means that they can adopt multiple conformational states with
51 different protofilament arrangements, curvature and extent of tube closure[2,3]. Transitions between
52 these states can be controlled by the nucleotide state of tubulin, by tubulin isoforms and
53 modifications, and by local mechanical strain and binding of proteins and drugs[2-4].

54 Taxol (the brand name of the drug paclitaxel) is a microtubule-targeting agent (MTA) that is
55 broadly used for cancer therapy[5-7]. Taxol stabilizes microtubules by binding to a luminally
56 exposed β-tubulin site, which is shared by other microtubule-stabilizing agents[6-8]. Taxol has been
57 shown to straighten individual microtubule protofilaments[9], and cryo-electron microscopy (cryo-
58 EM) analysis indicated that Taxol allosterically affects longitudinal interfaces between tubulin
59 dimers by counteracting microtubule lattice compaction induced by GTP hydrolysis[10-12].
60 Furthermore, analysis of MTA interactions with unpolymerized tubulin showed that some taxane-
61 site ligands, such as epothilone A, affect the structure of the β-tubulin M-loop, which contributes
62 to the lateral interactions between tubulin dimers[13-15]. The notion that taxane-site binding
63 compounds stabilize lateral tubulin interactions is supported by a recent cryo-EM study[16]. While
64 these structural insights explain how these MTAs stabilize microtubules at saturating
65 (micromolar) concentrations, they do not account for the drug effects at lower concentrations,
66 which potently suppress both microtubule growth and shortening[5]. Understanding such effects is
67 of crucial importance, because they represent the clinically relevant situation as the concentration
68 of Taxol in plasma during chemotherapy was estimated to be in the range between tens and a few
69 hundred nanomolar[17-20].

Our previous work has shown that non-saturating Taxol concentrations (50-100nM) can promote catastrophes induced *in vitro* by the End Binding (EB) family proteins[21]. Catastrophe potentiation by low Taxol concentrations is readily observed in cells (for an example, see[22]). In line with these data, low concentrations of Taxol and microtubule-destabilizing vinca alkaloids synergize rather than counteract each other in inhibiting cancer cell proliferation[23], in spite of having seemingly opposite mechanisms of action. Low Taxol concentrations thus do not increase overall microtubule stability; however, they do cause formation of discrete sites that block microtubule shrinkage and induce repeated rescues[21]. To understand how such rescue sites are formed, we visualized drug binding during microtubule growth using fluorescent taxane-site ligands. We found that these MTAs cooperatively bind to microtubule tips that are in a pre-catastrophe state and convert them into islands of stabilized microtubule lattice .

Taxane accumulations induce repeated microtubule rescues

To directly visualize the effects of taxanes on microtubule dynamics, we used two green fluorescent Taxol derivatives, Fchitax-3 and Flutax-2 [24,25] (Supplementary Fig. 1a). We used a Total Internal Reflection Fluorescence microscopy (TIRFM)-based assay, in which microtubule seeds stabilized with the slowly hydrolysable GTP analogue GMPCPP are extended in the presence of soluble tubulin with or without other proteins or drugs[21,26] (Supplementary Fig. 1b,c). Whereas almost no rescues occurred either with tubulin alone or in the presence of mCherry-EB3, we observed frequent rescues in the presence of Taxol and its fluorescent derivatives (Fig. 1a-d, Supplementary Fig. 1c-e). As described previously[21], these rescues typically happened at defined microtubule lattice sites, which we termed “stable rescue sites” (Fig. 1a-c, Supplementary

Fig. 1d). Importantly, in the case of fluorescent taxanes, we observed a ~4 fold enhanced drug binding at such sites as compared to the rest of the microtubule lattice (Fig. 1b,c). Similar sites with increased drug accumulation inducing repeated rescues could also be detected in HeLa cells that expressed EB3-TagRFP as a microtubule plus-end marker and were incubated with 100nM Fchitax-3 for 1hr (Fig. 1e). Comparison of the intensities of single Fchitax-3 molecules and of very short Fchitax-3 accumulations at the stable rescue sites in vitro showed that they contained ~15 molecules (Supplementary Fig. 1f-j). Taxane-induced formation of stable rescue sites thus occurs both in vitro and in cells, and ~15 drug molecules are sufficient to induce such a site.

Taxane accumulations initiate at microtubule ends

While observing microtubule growth in the presence of fluorescent taxanes, we noticed that the compounds always started to accumulate close to the growing microtubule plus or minus ends, directly behind the EB3-positive comet (Fig. 2a,b, Supplementary Fig. 2a, Supplementary Video 1). Taxane accumulation events appeared in a stochastic manner (Supplementary Fig. 2b) and were somewhat more prolonged and more frequent at the minus ends (Fig. 2a,b, Supplementary Fig. 2a,c). For subsequent work, we focused on drug accumulations at the plus ends, as minus ends typically do not elongate much in vivo[27]. Consistent with the in vitro data, transient accumulations of Fchitax-3 were also observed at growing microtubule plus ends in cells (Supplementary Fig. 2d,e).

To test whether end-dependent binding was specific for Taxol analogues, we generated an Alexa-488-labeled derivative of epothilone B (Supplementary Fig. 1a, Supplementary Fig. 3a,b), a different taxane-site binder, and found that it exhibited similar accumulations at growing

microtubule ends (Fig. 2c). The drug accumulations also occurred in the absence of EB3 (Fig. 2d, Supplementary Fig. 2f); however, since EBs facilitate the detection of growing microtubule tips, subsequent experiments were carried out in the presence of EB3. During periods of strong drug accumulation, microtubule growth was perturbed, as could be seen by the reduction of EB3 signal and the microtubule growth rate (Fig. 2a,c-g). After a brief interval, an accumulation could abruptly stop and normal microtubule growth could resume (Fig. 2a,c-g). Concomitantly, the region of enhanced drug binding persisted in the microtubule lattice (Fig. 2a,c,d). If such a growing microtubule started shrinking, microtubule depolymerization was arrested within the region with a high drug concentration, leading to rescue, which was often observed repeatedly at the same site (Fig. 2a,c, Supplementary Fig. 2a). Microtubule polymerization with periods of perturbed growth and subsequent frequent rescues initiating within the same microtubule region was also observed with Taxol, with and without EB3 (Supplementary Fig. 2g,h). Such a behavior is thus representative for taxane-site MTAs and is not an artifact of fluorescently labeled drugs.

To confirm that regions with high taxane accumulation have an increased stability, we performed laser severing experiments. Whereas control microtubules always depolymerized at the newly generated plus- and minus-ends (Supplementary Fig. 2i), the presence of an Fchitax-3 accumulation prevented shrinkage of freshly severed ends (Fig. 2h, Supplementary Video 2). These data demonstrate that increased taxane incorporation initiated close to a growing microtubule end leads to stabilization of a stretch of microtubule lattice.

Taxane accumulations are triggered by growth perturbations

135 Since microtubule minus ends grow slower than plus ends and show longer and more frequent
136 Fchitax-3 accumulations (Supplementary Fig. 1c, 2c), we initially hypothesized that the drugs can
137 accumulate more easily at their luminal binding sites if microtubule polymerization is slow.
138 However, when we varied tubulin concentration to alter the growth speed (Supplementary Fig.
139 4a,b), we found that in fact Fchitax-3 accumulations became more frequent when microtubules
140 grew faster (Fig. 3a,b, Supplementary Fig. 4c). At higher growth rates, the length of Fchitax-3
141 accumulations increased (Fig. 3a,b, Supplementary Fig. 4c). In our assays, in the presence of EB3
142 without MTAs, increased tubulin concentrations led to a higher catastrophe frequency, although
143 at 25μM tubulin, we did observe some microtubules that were persistently elongating
144 (Supplementary Fig. 4a); importantly, such microtubules still displayed frequent growth
145 perturbations that appeared as a catastrophe followed by a rapid rescue (Supplementary Fig.
146 4a,b).

147 Interestingly, we noticed that Fchitax-3 accumulations were often initiated when microtubule
148 polymerization appeared suboptimal or perturbed, which was often observed at microtubule
149 minus ends (Supplementary Fig. 1c, Fig. 2b), or when the plus end of a GMPCPP seed just
150 started to elongate (Supplementary Fig. 4d). Fchitax-3 accumulation events were always
151 accompanied by a decrease in microtubule growth rate and the concomitant loss in EB3 signal
152 (Fig. 2e-g). Analysis of the onset of such events with a higher temporal resolution and careful
153 alignment of the Fchitax-3 and EB3 channels showed that on processively growing microtubules,
154 the appearance of a new Fchitax-3 accumulation occurred ~5s after a clear reduction in EB3
155 signal (Fig. 3c-e). The reduction in the number of EB3-binding sites at the growing microtubule
156 end is a hallmark of the pre-catastrophe state[28] (Supplementary Fig. 4e). Furthermore, the

157 frequencies of catastrophes and of appearance of Fchitax-3 accumulations at the growing
158 microtubule ends are similar (Supplementary Fig. 4f).

159 We therefore wondered whether Fchitax-3 accumulations could be triggered by changes in the
160 microtubule end conformation that lead to catastrophe. Catastrophes can be potently stimulated in
161 our in vitro assays by different microtubule-depolymerizing agents, such as vinblastine[21] or by
162 kinesin-13 family protein mitotic centromere-associated kinesin (MCAK)[29]. The addition of
163 GFP-MCAK, which specifically tracked growing EB3-positive microtubule ends, or vinblastine
164 reduced microtubule growth rate and indeed promoted catastrophes (Supplementary Fig. 4g).
165 These conditions are somewhat reminiscent of the dynamics of microtubule minus ends, which
166 exhibit frequent growth perturbations (Supplementary Fig. 1c, 4g). Interestingly, the addition of
167 vinblastine or GFP-MCAK increased the frequency of Fchitax-3 or $Alexa_{488}$-epothilone B
168 accumulations, as well as the occurrence of stable rescue sites with or without EB3 (Fig. 3f-i,
169 Supplementary Fig. 4h,i). A similar pattern of microtubule plus end growth with frequent
170 perturbations and repeated rescues was also observed with the combination of vinblastine and
171 Taxol (Fig. 3j), indicating that the behavior of fluorescent compounds is representative for
172 taxane-site binders. It should be emphasized that vinblastine can bind to free tubulin and to the
173 outmost microtubule tips[30], but cannot be incorporated into microtubule lattices and directly
174 influence the conformation of the taxane-binding site within microtubule shafts. MCAK also acts
175 at the outmost microtubule tips and is not expected to influence microtubule lattice structure[31].
176 Together, these data show that the perturbed structure of a microtubule end associated with the
177 pre-catastrophe state induces formation of lattice regions with enhanced taxane accumulation.

178

Analysis of Fchitax-3 binding kinetics

To understand better how Fchitax-3 accumulations are formed, we analyzed their dynamics in more detail. After the binding was initiated, Fchitax-3 intensity on the microtubule first rapidly increased over the course of ~50s, and then, after a period of ~100s, it abruptly started to diminish (Fig. 4a). The rapid decline of Fchitax-3 intensity within the accumulation zone was not caused by photobleaching (Supplementary Fig. 5a, see figure legend for details), and thus was due to drug dissociation from the microtubule.

The shape of the kinetic curve, with a rapid rise and a subsequent decline, suggests that some tubulin dimers first acquire an ability to bind Fchitax-3 (the initial drug accumulation phase), but later are converted to a state lacking this ability (the drug desorption phase). Because Fchitax-3 binding does not happen throughout the entire period of microtubule growth, but emerges at the ends that are in a pre-catastrophe state, we defined two subsets of tubulins present at microtubule ends, which have different ability to interact with Fchitax-3: $Tu^{receptive}$ and $Tu^{unreceptive}$. To account for desorption, we assumed that these states can be turned into the microtubule lattice-specific conformational state that does not bind to Taxol in these conditions ($Tu^{lattice}$).

To model the kinetics of Fchitax-3 accumulation and unbinding, we first used a Michaelis-Menten type of model, in which Taxol was taken as a 'catalyst' that binds $Tu^{receptive}$ (the ''substrate') that subsequently converts irreversibly to a non-Taxol-binding state within the microtubule lattice ($Tu^{lattice}$, the 'product'). However, this model provided a poor fit to experimentally obtained binding curve (Fig. 4b,c, Supplementary Fig. 5b,c). To account for the rapid and sustained increase in drug accumulation, we introduced an autocatalytic step (Fig. 4b), in which binding of Taxol to $Tu^{receptive}$ can trigger the conversion of unreceptive tubulin at

201 microtubule ends to receptive tubulin (Fig. 4a-c, Supplementary Fig. 5d-g, see Methods for
202 details). The obtained rate constant of Fchitax-3 binding (k_1, 5.6±0.5 x10^5 $M^{-1}s^{-1}$) was in good
203 agreement with previously reported measurements for Flutax-1 and Flutax-2 [24,32], whereas the
204 rate constant of dissociation was an order of magnitude lower (k_{-1}, 1.4±0.2 x10^{-2} s^{-1}, Fig. 4d). This
205 is consistent with the fact that the affinity of Fchitax-3 for its binding site is an order of
206 magnitude higher than that of Flutax-2 [24,25].

207 Next, we explored how the kinetic parameters changed along the length of the microtubule zone
208 where an accumulation happened. In our dynamics assays, the maximum Fchitax-3 intensity
209 observed over time was typically higher at the initial point of the accumulation compared to its
210 distal end, which was formed later (Fig. 4a). In the model, this was reflected by the diminishing
211 number of tubulin dimers per unit of microtubule length that could interact with the drug
212 (Supplementary Fig. 5d). Furthermore, FRAP data showed that the recovery of Fchitax-3 at the
213 starting point of an accumulation was higher compared to the distal end of an accumulation (Fig.
214 4e), and this fitted well with the modeling results (Fig. 4c,f). The higher number of drug binding
215 sites at the starting point of Fchitax-3 accumulation was in agreement with the observation that
216 this region was often most resistant to depolymerization (see Fig. 3c for an example). Thus, the
217 conformation of the microtubule zone with a high taxane affinity was changing along the
218 growing microtubule. This could be due to some global alterations in microtubule geometry, such
219 as a gradual closure of an open tubulin sheet. In the model, this was reflected by the variability of
220 the autocatalysis rate constant k_2 (Fig. 4d), which can be expected to be affected by tubulin
221 conformation in the microtubule lattice.

222 Quantification of the density of Fchitax-3 molecules during maximal accumulation along
223 microtubule stretches of ~900nm length showed that ~1-2 drug molecules were bound per 8nm,

the length of one tubulin dimer (Supplementary Fig. 5h). Since GMPCPP-nucleated microtubules in our assays are expected to have ~14 protofilaments, this means that even at the highest binding density the microtubule is still far from being saturated with the drug. It should be noted that since this quantification is based on the average fluorescence intensity, it is possible that Fchitax-3 molecules are distributed in an irregular fashion, for example, with neighboring tubulin subunits being preferentially in either bound or unbound state. Combined with the modeling, our data suggest that taxanes display cooperative binding to microtubules even at low saturation, suggesting that changes in drug binding affinity can propagate in microtubule lattices.

Nucleotide state of tubulin affects Fchitax-3 binding

Since growing microtubule ends maintain a GTP cap that is gradually hydrolyzed, and since tubulin undergoes nucleotide-dependent conformational changes[10,16,33], enhanced Fchitax-3 binding at growing microtubule tips could be due to a particular nucleotide state. Fchitax-3 and other tested taxanes indeed showed preference for GMPCPP seeds and GMPCPP-containing microtubule extensions as compared to GDP-bound lattices (Fig. 5a,b). FRAP analysis of Fchitax-3 signal on GMPCPP seeds provided an estimate for the dissociation constant (k_{-1} FRAP, $2.2\pm0.3 \times 10^{-2}\ s^{-1}$), which was similar to the values derived from our autocatalysis kinetic model (Fig. 5c,d). In contrast, Fchitax-3 had no preference for GTPγS-bound microtubules, which are thought to mimic the GTP-Pi state of tubulin[11,33] (Fig. 5e).

Preferential binding to GMPCPP microtubules might be due to their longitudinally extended lattice conformation, because Taxol was reported to induce similar microtubule lattice extension if added during though not after microtubule assembly[11,16,33,34]. To get support for the idea that

Taxol affects tubulin dimer length within microtubules, we performed X-ray fiber diffraction experiments with microtubules that were assembled from GTP-tubulin and were either untreated or treated with Taxol during or after polymerization (Supplementary Fig. 6a-e). Both Taxol-treated samples exhibited an increased dimer length compared to drug-free microtubules, though this length was slightly shorter in samples treated with Taxol after assembly (Supplementary Fig. 6f,g). Similarly, microtubules assembled from GDP-tubulin incubated with Taxol during polymerization also displayed extended lattice (Supplementary Fig. 6d-g) (note that GDP-tubulin does not polymerize without Taxol and, therefore, the effect of Taxol could not be tested in the post-assembly conditions). Taxol can thus induce changes in microtubule lattice compaction that could contribute to the observed binding preferences and cooperativity. However, the maximum intensity of Fchitax-3 accumulations at microtubule ends greatly exceeded the intensity of the drug binding to GMPCPP-stabilized seeds present in the same microtubules (Fig. 5a). Furthermore, Fchitax-3 accumulations could also form at microtubule tips in the presence of GTPγS, although in this case their intensity was typically lower than that at GMPCPP-containing microtubule seeds in the same assay (Fig. 5e). We therefore conclude that the nucleotide state of tubulin and the associated changes in the longitudinal lattice compaction can affect taxane binding, but they are not sufficient to explain the strong drug accumulations at microtubule ends. In particular, rapid release of Fchitax-3 from the accumulation zones and the abrupt transitions between regions of high and low drug binding can be best explained by additional global conformational transitions, such as the closure of a microtubule sheet into a tube.

Taxanes induce tube closure defects

268 To investigate whether the presence of taxane accumulations is indeed associated with deviations
269 in microtubule structure, we performed a cryo-EM analysis of GMPCPP-stabilized microtubule
270 seeds, control microtubules, microtubules grown in the presence of either Fchitax-3 or
271 vinblastine, or both agents together (Fig. 6a-d, Supplementary Fig. 7a-c). GMPCPP stabilized
272 microtubule seeds showed a regular geometry with very few, small defects (< ~40nm)
273 (Supplementary Fig. 7a). Whereas Fchitax-3 had no effect on the abundance of small microtubule
274 defects (<~40nm), we observed in its presence a significant increase in the frequency of
275 incomplete microtubule shaft regions that were longer than 40nm (Fig. 6a-d). Very long regions
276 of incomplete microtubule lattices were seen when Fchitax-3 and vinblastine were combined
277 (Supplementary Fig. 7b,c). These data strongly suggest that the regions of enhanced Fchitax-3
278 binding represent microtubule regions that failed to close into a complete microtubule tube.

279 Incomplete microtubule lattice structures are expected to show increased flexibility, and we
280 indeed observed a strong increase in transverse microtubule tip fluctuations during formation of
281 Fchitax-3 accumulations (Fig. 6e). It should be noted that Taxol binding can by itself reduce
282 microtubule rigidity[34-36], and it is possible that this effect contributes to the flexible character of
283 the Fchitax-3 accumulation zones.

284 To confirm that Fchitax-3-grown microtubules contain interrupted protofilaments, we used as a
285 tool the microtubule minus-end binding protein CAMSAP3. CAMSAPs recognize free
286 microtubule minus ends because their signature domain, CKK, binds in a minus-end specific
287 manner to interprotofilament sites at uncapped microtubule extremities[37]. Interestingly, distinct
288 CAMSAP3 binding was observed at ~30% of Fchitax-3 accumulations (Fig. 6f, Supplementary
289 Fig. 7d). Over time, the CAMSAP3 signal extended in the minus end direction (Fig. 6f). Since
290 CAMSAPs decorate growing microtubule minus ends[38], these data indicate that Fchitax-3

291 accumulations can create regions of incomplete microtubule lattice that can be extended by
292 tubulin addition. These data also explain why Fchitax-3 accumulation zones can serve as origin
293 of EB3-positive comets (Fig. 3f,h, white arrows in EB3 panels), which highlight growing
294 protofilament plus- and minus-ends. Similar events were also observed in the presence of Taxol
295 (Fig. 3i, white arrows).

296 Next, we used fluorescence recovery after photobleaching (FRAP) assays in the tubulin channel
297 to test for tubulin incorporation at the Fchitax-3 accumulation zones. Whereas control
298 microtubule lattices showed no fluorescence recovery (Supplementary Fig. 7e), Fchitax-3
299 accumulation zones displayed clear recovery of the tubulin signal (Fig. 6g). In some cases, the
300 length of tubulin incorporation detected after photobleaching was up to ~1μm (Supplementary
301 Fig. 7f). We also frequently observed transient binding of EB3, a marker of growing microtubule
302 ends, within the drug accumulation areas (Fig. 6h, Supplementary Fig. 7g). These data indicate
303 that tubulin indeed incorporates into microtubule lattice within Fchitax-3 accumulation zones.
304 Such microtubule repair explains why the length of microtubule lattice defects observed by EM
305 (~100nm) was much shorter than the length of Fchitax-3 accumulation zones, which could extend
306 to several micrometers (compare Fig. 6d and Supplementary Fig. 7h). These results indicate that
307 formation of Fchitax-3 accumulations is associated with major microtubule lattice defects such as
308 missing parts of protofilaments that are partly restored by tubulin incorporation.

309

Discussion

In this study, we found that the association of taxane-site ligands with microtubules preferentially occurs at growing microtubule ends and strongly depends on the conformational state of these ends, leading to a highly uneven binding pattern along the microtubule shaft. This observation helps to explain why taxane-site ligands have a stronger effect on the microtubule lattice structure when added during and not after microtubule polymerization[34,39]. Previous models of Taxol stabilization mechanisms assumed a stochastic but homogeneous change in the rate constants and thermodynamic states of tubulin dimers inside a microtubule[40]. In contrast, our data show that at non-saturating concentration of the compound, microtubule stabilization is achieved by the formation of specific zones (local "clusters") with an increased stability, possibly due to a cooperative change in the microtubule lattice structure. The formation of local clusters is reminiscent of polymorphic transitions in crystals, suggesting that the addition of a taxane-site ligand to dynamic microtubules induces altered forms of microtubule lattices.

The nucleotide state of tubulin plays a role in controlling taxane affinity for microtubules, with the GMPCPP-bound, extended conformation being preferred over the compacted GDP or GTPγS lattice, consistent with the data that both GMPCPP- and Taxol-bound microtubules have expanded lattice[10,33,34]. However, the pattern of ligand binding to a growing microtubule cannot be explained by the nucleotide state of tubulin alone. Our data suggest that taxane-site ligands can preferentially bind to incomplete microtubule structures present at the ends and strongly modify the properties of these structures (Fig. 6i). The increased affinity of taxanes for incomplete tubulin structures, such as tubulin sheets, can explain their binding kinetics: as long as the tube is incomplete, taxane keeps binding, but if the sheet closes into a tube, a significant proportion of the drug molecules is released. Our data are consistent with the idea that, after tube

333 closure and growth continuation, an open structure remains at the initial part of the drug
334 accumulation zone, explaining why the drug can still exchange within this region and create a
335 stable site that inhibits microtubule depolymerization. Incorporation of GTP-tubulin at the drug
336 accumulation zones promotes their stability and their capacity to induce rescues, as described
337 previously for other situations where microtubule lattice repair has been observed[41-43].
338 Importantly, our data suggest that microtubule repair at the drug accumulation sites is not
339 complete – a part of the microtubule lattice remains open, but is not depolymerized due to the
340 presence of drug molecules.

341 An interesting feature of taxane binding to microtubule lattices is its cooperative character. Our
342 modeling based on the kinetic binding curves suggests that initially only a few tubulin dimers
343 within the microtubule lattice can bind the drug, and that drug association catalyzes formation of
344 additional binding sites in the vicinity. One potential explanation of such cooperativity could be
345 based on the propagation of an extended conformational state of the microtubule lattice, which
346 was observed for Taxol-bound microtubules by cryo-EM[10,33,34] and in our X-ray fiber diffraction
347 experiments. A similar elongation of the axial microtubule repeat has recently been proposed to
348 underlie the positive cooperativity in the binding of kinesin-1 to microtubules[44]. However, since
349 taxane-site ligands can also affect lateral contacts between tubulin dimers[13-16], it is possible that
350 alterations in these contacts account for propagating structural effects, such as a differential
351 curvature of tubulin sheets.

352 Taxane-bound zones at microtubule ends represent suboptimal substrates for microtubule
353 shrinkage but also for microtubule growth. This leads to slow growth and frequent transitions
354 between growth and shortening, which help to explain the surprising observation that although

355 Taxol is a microtubule stabilizer, at low concentrations it perturbs microtubule growth in cells
356 (reviewed in[45], see[22] for an example).

357 An important conclusion of our study is that the conformational transitions at microtubule ends,
358 which lead to growth perturbation and catastrophes also promote taxane-site ligand binding and
359 microtubule stabilization by these compounds. One interesting consequence of this effect is that
360 the distribution of ligand accumulations along the microtubule shaft reflects the history of the
361 growth of this microtubule. Another important consequence is that taxane-site ligand binding to
362 microtubules can be potentiated by low doses of catastrophe-inducing MTAs, and some evidence
363 supporting this idea has already been reported based on cell culture experiments[23]. Our data
364 provide an explanation for this phenomenon and suggest that in future work it can be exploited
365 for optimizing MTA-based cancer therapies.

366

References

1. Desai, A. & Mitchison, T.J. Microtubule polymerization dynamics. *Annu Rev Cell Dev Biol* **13**, 83-117 (1997).
2. Cross, R.A. Microtubule lattice plasticity. *Curr Opin Cell Biol* **56**, 88-93 (2018).
3. Kueh, H.Y. & Mitchison, T.J. Structural plasticity in actin and tubulin polymer dynamics. *Science* **325**, 960-963 (2009).
4. Brouhard, G.J. & Rice, L.M. Microtubule dynamics: an interplay of biochemistry and mechanics. *Nat Rev Mol Cell Biol* **19**, 451-463 (2018).
5. Dumontet, C. & Jordan, M.A. Microtubule-binding agents: a dynamic field of cancer therapeutics. *Nat Rev Drug Discov* **9**, 790-803 (2010).
6. Yang, C.H. & Horwitz, S.B. Taxol((R)): The First Microtubule Stabilizing Agent. *Int J Mol Sci* **18**, E1733 (2017).
7. Steinmetz, M.O. & Prota, A.E. Microtubule-Targeting Agents: Strategies To Hijack the Cytoskeleton. *Trends Cell Biol* **28**, 776-792 (2018).
8. Nogales, E. & Kellogg, E.H. Challenges and opportunities in the high-resolution cryo-EM visualization of microtubules and their binding partners. *Curr Opin Struct Biol* **46**, 65-70 (2017).
9. Elie-Caille, C. *et al.* Straight GDP-tubulin protofilaments form in the presence of taxol. *Curr Biol* **17**, 1765-1770 (2007).
10. Alushin, G.M. *et al.* High-resolution microtubule structures reveal the structural transitions in alphabeta-tubulin upon GTP hydrolysis. *Cell* **157**, 1117-1129 (2014).
11. Zhang, R., Alushin, G.M., Brown, A. & Nogales, E. Mechanistic Origin of Microtubule Dynamic Instability and Its Modulation by EB Proteins. *Cell* **162**, 849-859 (2015).

390 12. Kellogg, E.H. *et al.* Near-atomic model of microtubule-tau interactions. *Science* **360**,
391 1242-1246 (2018).
392 13. Prota, A.E. *et al.* Molecular mechanism of action of microtubule-stabilizing anticancer
393 agents. *Science* **339**, 587-590 (2013).
394 14. Prota, A.E. *et al.* Structural Basis of Microtubule Stabilization by Discodermolide.
395 *Chembiochem* **18**, 905-909 (2017).
396 15. Wang, Y. *et al.* Mechanism of microtubule stabilization by taccalonolide AJ. *Nat*
397 *Commun* **8**, 15787 (2017).
398 16. Manka, S.W. & Moores, C.A. The role of tubulin-tubulin lattice contacts in the
399 mechanism of microtubule dynamic instability. *Nat Struct Mol Biol* **25**, 607-615 (2018).
400 17. Brown, T. *et al.* A phase I trial of taxol given by a 6-hour intravenous infusion. *J Clin*
401 *Oncol* **9**, 1261-1267 (1991).
402 18. Weaver, B.A. How Taxol/paclitaxel kills cancer cells. *Mol Biol Cell* **25**, 2677-2681
403 (2014).
404 19. Gianni, L. *et al.* Nonlinear pharmacokinetics and metabolism of paclitaxel and its
405 pharmacokinetic/pharmacodynamic relationships in humans. *J Clin Oncol* **13**, 180-190
406 (1995).
407 20. Spratlin, J. & Sawyer, M.B. Pharmacogenetics of paclitaxel metabolism. *Crit Rev Oncol*
408 *Hematol* **61**, 222-229 (2007).
409 21. Mohan, R. *et al.* End-binding proteins sensitize microtubules to the action of microtubule-
410 targeting agents. *Proc Natl Acad Sci U S A* **110**, 8900-8905 (2013).
411 22. Bouchet, B.P. *et al.* Mesenchymal Cell Invasion Requires Cooperative Regulation of
412 Persistent Microtubule Growth by SLAIN2 and CLASP1. *Dev Cell* **39**, 708-723 (2016).

413 23. Photiou, A., Shah, P., Leong, L.K., Moss, J. & Retsas, S. In vitro synergy of paclitaxel
414 (Taxol) and vinorelbine (navelbine) against human melanoma cell lines. *Eur J Cancer* **33**,
415 463-470 (1997).
416 24. Diaz, J.F., Strobe, R., Engelborghs, Y., Souto, A.A. & Andreu, J.M. Molecular
417 recognition of taxol by microtubules. Kinetics and thermodynamics of binding of
418 fluorescent taxol derivatives to an exposed site. *J Biol Chem* **275**, 26265-26276 (2000).
419 25. Li, X., Barasoain, I., Matesanz, R., Diaz, J.F. & Fang, W.S. Synthesis and biological
420 activities of high affinity taxane-based fluorescent probes. *Bioorg Med Chem Lett* **19**,
421 751-754 (2009).
422 26. Bieling, P. *et al.* Reconstitution of a microtubule plus-end tracking system in vitro. *Nature*
423 **450**, 1100-1105 (2007).
424 27. Akhmanova, A. & Steinmetz, M.O. Control of microtubule organization and dynamics:
425 two ends in the limelight. *Nat Rev Mol Cell Biol* **16**, 711-726 (2015).
426 28. Duellberg, C., Cade, N.I., Holmes, D. & Surrey, T. The size of the EB cap determines
427 instantaneous microtubule stability. *Elife* **5**, e13470 (2016).
428 29. Montenegro Gouveia, S. *et al.* In Vitro Reconstitution of the Functional Interplay between
429 MCAK and EB3 at Microtubule Plus Ends. *Curr Biol* **20**, 1717-1722 (2010).
430 30. Gigant, B. *et al.* Structural basis for the regulation of tubulin by vinblastine. *Nature* **435**,
431 519-522 (2005).
432 31. Friel, C.T. & Welburn, J.P. Parts list for a microtubule depolymerising kinesin. *Biochem*
433 *Soc Trans* **46**, 1665-1672 (2018).
434 32. Diaz, J.F., Barasoain, I. & Andreu, J.M. Fast kinetics of Taxol binding to microtubules.
435 Effects of solution variables and microtubule-associated proteins. *J Biol Chem* **278**, 8407-
436 8419 (2003).

437 33. Zhang, R., LaFrance, B. & Nogales, E. Separating the effects of nucleotide and EB
438 binding on microtubule structure. *Proc Natl Acad Sci U S A* **115**, E6191-E6200 (2018).
439 34. Kellogg, E.H. *et al.* Insights into the Distinct Mechanisms of Action of Taxane and Non-
440 Taxane Microtubule Stabilizers from Cryo-EM Structures. *J Mol Biol* **429**, 633-646
441 (2017).
442 35. Mitra, A. & Sept, D. Taxol allosterically alters the dynamics of the tubulin dimer and
443 increases the flexibility of microtubules. *Biophys J* **95**, 3252-3258 (2008).
444 36. Kikumoto, M., Kurachi, M., Tosa, V. & Tashiro, H. Flexural rigidity of individual
445 microtubules measured by a buckling force with optical traps. *Biophys J* **90**, 1687-1696
446 (2006).
447 37. Atherton, J. *et al.* A structural model for microtubule minus-end recognition and
448 protection by CAMSAP proteins. *Nat Struct Mol Biol* **24**, 931-943 (2017).
449 38. Jiang, K. *et al.* Microtubule minus-end stabilization by polymerization-driven CAMSAP
450 deposition. *Dev Cell* **28**, 295-309 (2014).
451 39. Arnal, I. & Wade, R.H. How does taxol stabilize microtubules? *Curr Biol* **5**, 900-908
452 (1995).
453 40. Castle, B.T. *et al.* Mechanisms of kinetic stabilization by the drugs paclitaxel and
454 vinblastine. *Mol Biol Cell* **28**, 1238-1257 (2017).
455 41. Schaedel, L. *et al.* Microtubules self-repair in response to mechanical stress. *Nat Mater*
456 **14**, 1156-1163 (2015).
457 42. Aumeier, C. *et al.* Self-repair promotes microtubule rescue. *Nat Cell Biol* **18**, 1054-1064
458 (2016).
459 43. Vemu, A. *et al.* Severing enzymes amplify microtubule arrays through lattice GTP-
460 tubulin incorporation. *Science* **361,** eaau1504 (2018).

461 44. Shima, T. *et al.* Kinesin-binding-triggered conformation switching of microtubules
462 contributes to polarized transport. *J Cell Biol* **217**, 4164-4183 (2018).
463 45. Jordan, M.A. & Wilson, L. Microtubules as a target for anticancer drugs. *Nat Rev Cancer*
464 **4**, 253-265 (2004).
465
466

Acknowledgements

We thank Ganadería Fernando Díaz for calf brains supply and staff of beamline BL11-NCD-SWEET (ALBA, Cerdanyola del Vallès, Spain) for their support with X-ray fiber diffraction experiment. We thank Prof. Dr. Shinji Kamimura (Chuo University, Tokyo, Japan) for kindly providing the share flow device employed for fiber diffraction experiments. This work was supported by the European Research Council Synergy grant 609822 and the Netherlands Organization for Scientific Research (NWO) CW ECHO grant 711.015.005 to A.A., by a Biotechnology and Biological Sciences Research Council (BBSRC, BB/N018176/1) grant to C.A.M., by an EMBO Long Term Fellowship to R. R.-G., by CAMS Innovation Fund for Medical Sciences (CIFMS), grant 2016-I2M-1-010 to W.-S.F., by grants from MINECO/FEDER (BFU2016-75319-R) to J.F.D, and by the COST Action grant CM1407 to J.F.D. and K.-H.A. M.O.S is supported by a grant from the Swiss National Science Foundation (31003A_166608).

Author Contributions

A.R. designed and performed experiments, analyzed data and wrote the paper. T.L. and C.A.M designed and performed cryo-EM experiments and analyzed the data; E.A. analyzed data and performed the modeling; J.E.G. performed X-ray fiber diffraction experiments; R.R.-G. analyzed microtubule tip fluctuation data; W.-S. F synthesized Fchitax-3 and Flutax-2, S.G. and K.-H.A. synthesized $Alexa_{488}$-Epothilone B; L.C.K, J.F.D. and M.O.S contributed to the design of the experiments and analysis of the data and models; A.A. designed experiments, coordinated the project and wrote the paper.

Competing financial interests

The authors declare no competing financial interests.

Figure legends

Figure 1: Taxol and its fluorescent derivatives induce formation of stable rescue sites in microtubules.

a-c) Schemes illustrate in vitro microtubule growth events observed during control conditions and in the presence of microtubule stabilizing drugs. Representative kymographs illustrate the dynamics of microtubules grown from GMPCPP seeds in the presence of 15μM tubulin and 20nM mCherry-EB3 without or with Taxol, Fchitax-3 or Flutax-2 (100nM), as indicated. A stable rescue site in (a) is highlighted by a stippled white line. Note the enhanced green fluorescence of Fchitax-3 or Flutax-2 at the stable rescue site (white arrow). Bar graphs (mean ± SD) show the quantification of Fchitax-3 (n=65, N=5 independent experiments) and Flutax-2 (n=45, N=3 independent experiments) intensity on GDP lattice and on stable rescue site. The values were normalized to the intensity of the GDP lattice. Error bars represent SD. ****p <0.00001, Mann–Whitney U-test.

d) Frequency of the occurrence (mean ± SD) of stable rescue sites (calculated per unit of microtubule length) at the indicated compound concentrations. ND, not detected. n = 25, 40 and 25 microtubules for 50, 100 and 200nM of Fchitax-3, respectively, n = 25 microtubules for Taxol and Flutax-2 each, 3 independent experiments. Error bars represent SD.

e) Still images, time-lapse images (corresponding to the white circle in the still image) and representative kymographs showing the formation of a dot-like Fchitax-3-accumualtion corresponding to a stable rescue site in a microtubule in a HeLa cell. Bar graph (mean ± SD) shows the quantification of occurrence of stable rescue sites in HeLa cells. n=200 and 426 kymographs from 20 cells each for control and Fchitax-3 (100nM) treated sample (N=4 independent experiments). Error bar represent SD; ND, not detected.

Figure 2: Taxane-site binding compounds accumulate at growing microtubule ends and perturb microtubule growth and depolymerization.

a-d) Kymographs, representative of 3 independent experiments, illustrating the accumulation of the indicated compounds at the microtubule plus- (a,c,d) or minus- (b) ends (white arrow in the merged panel) in the presence of 15µM tubulin and 100nM Fchitax-3 or $Alexa_{488}$-Epothilone B, as indicated, with or without 20nM mCherry-EB3. In (d), 3% rhodamine-tubulin was added to the assay.

e,f) Fluctuations of fluorescence intensities (mean ± SD) of mCherry-EB3 at microtubule tips over time in control assays (15µM tubulin, 20nM mCherry-EB3) or in the presence of 100nM Fchitax-3, before or during the course of Fchitax-3 accumulation. (e), intensity distributions, with the experimental data shown by solid lines, and Gaussian fits by dotted lines, n=30 for control and n=25 for Fchitax-3 treated sample, N=3 independent experiments. (f), plots of the mean and SD values of the Gaussian fits.

g) Microtubule growth rate (mean ± SD) in the presence of 15µM tubulin, 20nM mCherry-EB3 and 100nM Fchitax-3 before, during and after an Fchitax-3 accumulation. n=51 in each case, N=3 independent experiments, error bars represent SD; ****$p<0.0001$ (growth rate during accumulation was compared with the rates before and after Fchitax-3 accumulation), Mann–Whitney U-test.

h) Schematic representation and still images of laser ablation of a microtubule with an Fchitax-3 accumulation zone, observed in the presence of 15µM tubulin (supplemented with 3% rhodamine tubulin), 20nM mCherry-EB3 and 100nM Fchitax-3. The ablated microtubule region is highlighted by a lightning bolt and white oval. The positions of the plus- and minus ends of the microtubule are indicated. Quantification (mean ± SD) of microtubule survival after the ablation

in control conditions (no drug) or within an Fchitax-3 accumulation zone (n=15 microtubules from 5 independent experiments) is shown on the right. ND = not detected.

Figure 3: Formation of accumulations of taxane-site ligands is controlled by microtubule dynamics.

a) Kymographs, representative of 3 independent experiments, showing Fchitax-3 accumulations in microtubules grown in the presence of the indicated tubulin concentrations, 20nM mCherry-EB3 and 100nM Fchitax-3.

b) Quantification of Fchitax-3 accumulation frequency (mean ± SD) for the experiments shown in (a). n = 15, 20, 40 and 37 accumulations in 250, 185, 135 and 94 growth events for 8, 10, 15 and 25µM of tubulin, respectively. N=3 independent experiments, error bars represent SD, ****p <0.0001, Mann–Whitney U-test.

c) Kymograph showing the initiation of an Fchitax-3 accumulation, associated with the reduction in mCherry-EB3 signal. N=5, experimental conditions as in (a).

d) Time plot of the normalized maximum intensity of a fitted EB3 comet (red) and the normalized area under the curve (AUC) of a fitted Fchitax-3 (green) intensity profile. The dashed green line shows the fit of Fchitax-3 kinetics to a Hill equation (on x-axis, time was used instead of concentration), representative of 5 experiments.

e) Averaged EB3 and Fchitax-3 profiles (same as in d), normalized and aligned using EC_{50} values from Hill equation fits as reference points (9 kymographs from 5 experiments).

f,h,i,j) Kymographs (representative of 3 experiments) illustrating microtubule dynamics in the presence of 15µM tubulin and indicated compounds and proteins. Note that GFP-MCAK at growing microtubule ends and Fchitax-3 accumulations are detected in the same channel. White

arrows highlight EB3 comets emerging from the accumulation zones and moving in the reverse direction.

g) Quantification of Fchitax-3 accumulation frequencies (mean ± SD) per microtubule unit length in the presence of 15μM tubulin (n=22), 20nM mCherry-EB3 (n=40), 15μM tubulin with 100nM vinblastine (n=25), 20nM mCherry-EB3 with 100nM vinblastine (n=30) and 20nM mCherry-EB3 with 5nM MCAK (n=34). n represents number of microtubules, N=3 independent experiments, error bars represent SD.

Figure 4: Analysis of the kinetics of Fchitax-3 accumulations.

a) Kymograph, representative of 5 independent experiments, with a long Fchitax-3 accumulation (left) and a line intensity time trace of Fchitax-3 at the beginning of the accumulation (right).

b) Schematic kinetic diagram of the Michaelis-Menten (top reaction) and autocatalysis (top and bottom reactions) models for Fchitax-3 binding. Three tubulin states are considered: initial [$Tu^{unreceptive}$] state unable to bind Fchitax-3, Fchitax-3 binding state [$Tu^{receptive}$] and final converted state [$Tu^{lattice}$] (again, unable to bind Fchitax-3). For more details see Methods.

c) Left: best fits to a single profile shown in (a) using Michaelis-Menten (red line) or the autocatalysis model (blue line). Right: raw data, best fits and residuals of the autocatalysis model to the area of the kymograph marked with a yellow rectangle in (a). Arrows 1 and 2 indicate the positions along the microtubule, for which FRAP was modeled in (f), with white dashes indicating the moments of photobleaching used for calculating the modeled curves.

d) Rate constants (mean ± SD) of kinetic autocatalysis model (b) derived from the intensity time trace fits (9 kymographs, 46 time traces total). Error bars represent SD.

e) Left panel: kymograph of three sequential photobleaching events (highlighted by black arrowheads) of an Fchitax-3 accumulation. Right panel: intensity time traces along the lines

marked by arrows 1 and 2 in the kymograph. Kymograph and intensity time traces are representative of 3 independent experiments.

f) Modeling of FRAP curves: solutions of the model for fluorescence recovery with parameter values from fits shown in (c) right panel, where the moments of photobleaching are indicated by white dashes. The same photobleaching moments are indicated by black arrowheads in (f).

Figure 5: Analysis of the nucleotide dependence of Fchitax-3 accumulations.

a) Fchitax-3 (100nM) fluorescence intensity profile on GMPCPP stabilized microtubule seed, dynamic microtubule lattice (GDP lattice) and within an Fchitax-3 accumulation. Bar graphs (mean values) show quantification of the normalized maximum value of fluorescence intensity on GMPCPP stabilized microtubule seed, GDP lattice and within an Fchitax-3 (n=50, N=5), Flutax-2 (n=34, N=3) or $Alexa_{488}$-Epothilone B (n=40, N=3) accumulation zone. The values were normalized to the intensity of the GDP lattice. Error bars represent SD. ****p <0.0001, Mann–Whitney U-test.

b) Kymographs illustrating in vitro dynamics of a microtubule that was first grown from a GMPCPP seed in the presence of 15µM tubulin and 20nM mCherry-EB3 (1), then in the presence of 5µM tubulin supplemented with 3% rhodamine tubulin and 250µM GMPCPP (GMPCPP cap) (2) and then incubated with 100nM Fchitax-3 (3). Fluorescence intensity profiles and the Fchitax-3 intensities (mean) normalized to the intensity of the GDP lattice are shown on the right. n=20, N=3 independent experiments. Error bars represent SD, ****p <0.0001, ns = not significant, p = 0.25, Mann–Whitney U-test.

c, d) Representative kymographs, single line intensity time traces and plot (mean value) showing the rate constant of photobleaching of Fchitax-3 within GMPCPP seeds. n=11, N = 5 independent

experiments. Error bar represents SD. Black arrowheads indicate the time point when photobleaching was performed.

e) Representative kymographs, intensity profiles and a plot (mean) showing the quantification of the intensity of Fchitax-3 fluorescence for GMPCPP-stabilized seed, microtubule lattice grown in the presence of 15µM tubulin, 20nM mCherry-EB3, 1mM GTPγS and 100nM Fchitax-3 (GTPγS lattice) and the Fchitax-3 accumulation zone within the same microtubule. Intensity values were normalized to the intensity of the GTPγS lattice. n=30 from N=3 independent experiments, error bars represent SD, ****p <0.0001, Mann–Whitney U-test.

Figure 6: Fchitax-3 promotes long sheet-like microtubule defects and generates sites of tubulin incorporation.

a,b) Cryo-EM images (representative of 2 experiments) of microtubules grown with 15µM tubulin and 20nM mCherry-EB3 without (a) or with (b) 100nM Fchitax-3. Long sheet-like defects are boxed.

c,d) Quantification of percentage of total defects (c) and defects with certain length (d) in GMPCPP stabilized microtubules, control (-Fchitax-3) (n=311 microtubules) and Fchitax-3 treated microtubules (+Fchitax-3) (n=833 microtubules), combined from 2 experiments each. ****p <0.0001; ns, no statistically significant difference, p=0.2, Pearson's chi-square test.

e) Top: time-lapse images illustrating that Fchitax-3 accumulation is accompanied by microtubule bending. Bottom left, an example of transverse microtubule tip fluctuations; bottom right, average standard deviation (normalized to the values before Fchitax-3 accumulation) of the microtubule tip fluctuations before, during and after an Fchitax-3 accumulation. n=11, N=5, **p=0.0038; ns, no statistically significant difference, p=0.55, Mann–Whitney U-test.

636 f) Left: kymographs illustrating microtubule dynamics with 15μM tubulin, 20nM GFP-EB3,
637 100nM Fchitax-3 and 10nM mCherry-CAMSAP3. Middle: a scheme illustrating CAMSAP3
638 binding to a microtubule minus end and protofilaments extending from an Fchitax-3
639 accumulation in the minus-end direction. Right: fluorescence intensity profiles and
640 quantifications (mean ± SD) showing CAMSAP3 intensity at the microtubule regions grown
641 from the minus (1) and plus (2) end of the seed and Fchitax-3 accumulation (3). Data were
642 normalized to the CAMSAP3 intensity of the microtubule grown from the minus end (2). n=10,
643 N=3 independent experiments.
644 g) Left: kymographs showing FRAP within microtubule region with Fchitax-3 accumulation.
645 White lightning bolt highlights the bleached region, and white arrowheads highlights tubulin
646 fluorescence recovery within bleached area. Middle: fluorescence intensity profiles of unbleached
647 and bleached microtubule regions with and without Fchitax-3 accumulation. Right: quantification
648 (mean ± SD) of tubulin fluorescence before, during and after photobleaching in control
649 microtubules (n=14) and microtubule regions with an Fchitax-3 accumulation (n=15), N=3
650 independent experiments. ****p <0.0001, , *p=0.1, Mann–Whitney U-test.
651 h) Quantification (mean ± SD) of EB3 fluorescence at growing plus ends or within microtubule
652 regions with or without an Fchitax-3 accumulation (n=30 microtubules from N=3 independent
653 experiments). Intensity values were normalized to the intensity of EB3 at growing microtubule
654 plus ends.****p <0.0001, Mann–Whitney U-test.
655 i) A model showing interaction of taxane-site ligands with microtubules. Taxanes show
656 preference for GMPCPP- over GDP-bound microtubule lattice. The onset of catastrophe
657 promotes taxane binding possibly due to end tapering and appearance of tubulin sheets. The
658 drugs exhibit binding cooperativity and stabilize these microtubule structures. Subsequently, the
659 regular microtubule structure is re-established due to tubulin incorporation; however, remnants of

660 an incomplete microtubule structure with a high drug affinity remain; they stabilize the site,
661 incorporate GTP-tubulin and promote repeated rescues.
662

Methods

Reagents and purified proteins

Taxol was purchased from Enzo Life Sciences. Vinblastine sulfate, GTP (Guanosine triphosphate), Glucose Oxidase from Aspergillus niger, Catalase from bovine liver, Methylcellulose, DTT (Dithiothreitol), PIPES (1,4-Piperazinediethanesulfonic acid, Piperazine-1,4-bis(2-ethanesulfonic acid), Piperazine-N,N′-bis(2-ethanesulfonic acid)), Magnesium chloride, EGTA (Ethylene glycol-bis(2-aminoethylether)-N,N,N′,N′-tetraacetic acid), Potassium hydroxide, Potassium chloride, κ-casein, Glucose, Fetal bovine serum, Penicillin-Streptomycin antibiotic were from Sigma-Aldrich. GMPCPP (Guanosine-5'-[(α,β)-methyleno]triphosphate, Sodium salt) was from Jena Biosciences. PLL-PEG-biotin (Biotinylated poly(L-lysine)-[g]-poly(ethylene glycol) was from Susos AG, Switzerland. NeutrAvidin was from Invitrogen. DMEM and F10 media, LT07-518 Mycoalert assay were from Lonza, Basel, Switzerland. Trysin-EDTA was from Biowest. FuGENE 6 was from Roche, Switzerland. Different types of labelled and unlabelled purified tubulin used in the assays were from Cytoskeleton, Denver, USA or purified as described previously[46] for fibre diffraction experiments. mCherry-CAMSAP3 and GFP-MCAK were purified as described previously[38, 47].

Synthesis of Alexa$_{488}$-Epothilone B

Alexa$_{488}$-Epothilone B was prepared by click reaction between an alkyne group-containing, C-6 modified epothilone B analog and an azide-containing derivative of Alexa 488. Alexa Fluor™ 488 Azide (2.18mg, 2.53µmol, 1.00eq) and C-6 modified epothilone B analog GS-240 (1.45mg, 2.53µmol, 1.00eq) were suspended in a mixture of *t*BuOH and water (1:1, 0.20ml). To this suspension Tris[(1-benzyl-1H-1,2,3-triazol-4-yl)methyl]amin (0.40mg, 0.758µmol, 0.30eq.) was

added and freshly prepared aqueous sodium ascorbate solution (1M solution in water, 2.5µl, 2.53µmol, 1.00eq) followed by an aqueous copper sulfate pentahydrate solution (0.8M, 0.6µl, 0.505µmol. 0.2eq). The reaction mixture was stirred for 4h at room temperature, until HPLC control showed complete conversion. The solvents were then removed under reduced pressure and the resulting residue was dissolved in a mixture of MeCN and water (1:2, 0.4ml) until a clear solution had formed. This solution was then directly purified by preparative HPLC (SymmetryPrep™ C18, 5µm, 19x100mm; MeCN: water 0:100 to MeCN: water 100:0 over 15 min, Retention time: 9.1min). Lyophilisation gave the compound $Alexa_{488}$-Epothilone B as a pink solid (2.71mg, 2.20µmol, 87%).

In vitro assay for microtubule dynamics

In vitro assay for microtubule growth dynamics was performed as described previously[29]. Briefly, as described earlier[48], GMPCPP stabilized microtubule seeds were prepared by two cycles of microtubule polymerization and depolymerization in the presence of GMPCPP (a slowly hydrolyzable GTP analog). A solution of porcine brain tubulin (20µM) mix containing biotin labeled-tubulin (18%) and rhodamine labeled-tubulin (12%) was polymerized in MRB80 buffer (80mM K-PIPES, pH 6.8, 4mM $MgCl_2$, 1mM EGTA) in the presence of GMPCPP (1mM) at 37°C for 30min. After polymerization, the mixture was pelleted by centrifugation in an Airfuge for 5min at 119,000 ×g. Obtained pellet was re-suspending in MRB80 buffer, depolymerized on ice for 20min and further polymerized in the presence of GMPCPP. After the second round of polymerization and pelleting, GMPCPP-stabilized microtubule seeds were stored in MRB80 containing 10% glycerol. In vitro flow chambers for TIRF microscopy were assembled on microscopic slides by two strips of double-sided tape with plasma-cleaned glass coverslips. Flow chambers were sequentially incubated with 0.2mg/ml PLL-PEG-biotin and 1mg/ml NeutrAvidin

in MRB80 buffer. Flow chambers were further incubated with GMPCPP stabilized microtubule seeds followed by treatment with 1mg/ml κ-casein. The reaction mixtures (15μM porcine brain tubulin supplemented with 3% rhodamine-tubulin when indicated, 20nM mCherry-EB3 or GFP-EB3 when indicated, 50mM KCl, 1mM guanosine triphosphate, 0.1% methylcellulose, 0.2mg/ml κ-casein and oxygen scavenger mixture (50mM glucose, 400μg/ml glucose oxidase, 200μg/ml catalase, and 4mM DTT in MRB80 buffer) with or without MTAs, GFP-MCAK or mCherry-CAMSAP3 were added to the flow chambers after centrifugation in an Airfuge for 5min at 119,000 ×g. Flow chambers were sealed with vacuum grease, and microtubule dynamics was recorded using TIRF microscopy. During in vitro sample imaging all samples were maintained at 30°C, cells were imaged at 37°C.

Cell culture

HeLa and HEK293T cells, obtained from ATCC, were cultured in DMEM/Ham's F10 media (1:1 ratio) supplemented with 10% fetal calf serum and 1% antibiotics (penicillin and streptomycin). ATCC performs short-tandem repeat profiling for cell line authentication, and no additional cell line authentication was performed. The cell line used here was not found in the database of commonly misidentified cell lines maintained by ICLAC. The cell line was routinely checked for mycoplasma contamination using LT07-518 Mycoalert assay. To determine the cellular effects of Fchitax-3, HeLa cells, transiently transfected with EB3-TagRFP (Grigoriev et al., 2008) using FuGENE 6, were treated with 100nM Fchitax-3 for 1hour. Cell imaging was performed using TIRF microscopy.

Image acquisition by TIRF microscopy and image analysis

Imaging was performed on a TIRF microscope setup (inverted research microscope Nikon Eclipse Ti-E) which was equipped with the perfect focus system (PFS) (Nikon) and Nikon CFI Apo TIRF 100x 1.49 N.A. oil objective (Nikon, Tokyo, Japan). The microscope was supplemented with TIRF-E motorized TIRF illuminator modified by Roper Scientific France/PICT-IBiSA Institut Curie, and a stage top incubator model INUBG2E-ZILCS (Tokai Hit) was used to regulate the temperature of the sample. Image acquisition was performed using either a Photometrics Evolve 512 EMCCD camera (Roper Scientific) or a Photometrics CoolSNAP HQ2 CCD camera (Roper Scientific) and controlled with MetaMorph 7.7 software (Molecular Devices, CA). For simultaneous imaging of red and green fluorescence we used triple-band TIRF polychroic ZT405/488/561rpc (Chroma) and triple-band laser emission filter ZET405/488/561m (Chroma), mounted in the metal cube (Chroma, 91032) together with Optosplit III beamsplitter (Cairn Research Ltd, Faversham, UK) equipped with double emission filter cube configured with ET525/50m, ET630/75m and T585LPXR (Chroma). Measurement of 491 nm laser power under TIRF conditions was performed using ThorLabs optical power and energy meter (PM400) unit using S170C sensor. Under TIRF conditions, maximum laser intensity (100% laser power) for 491 nm laser was found to be 160µW.

ImageJ plugin KymoResliceWide v.0.4 (https://github.com/ekatrukha/KymoResliceWide (Katrukha, 2015)) was used for generating kymographs to represent the life history of microtubule dynamics. As described previously[21,29], microtubule dynamics parameters from kymographs were determined with an optimized version of the custom-made JAVA plugin for ImageJ. For catastrophe frequency quantification, short depolymerization events (as depicted in Supplementary Fig. 4a, white arrow) were also considered as a catastrophe event.

Single molecule intensity analysis

To estimate the fluorescence intensity of single molecules of Fchitax-3, two parallel flow chambers were made on the same coverslip. In one chamber, regular microtubule dynamic assay in the presence of GMPCPP stabilized microtubule seeds with tubulin, mCherry-EB3 and Fchitax-3 was performed. The other chamber was incubated with the same concentration of Fchitax-3 without the reaction mixture. In both conditions, the first 10-20 images of unexposed coverslip areas were acquired with the 100ms exposure time using low laser intensity and then a movie of 10-20 frames exposing the same area with continuous laser illumination was recorded to induce photobleaching of Fchitax-3 molecules. Fluorescence intensities of Fchitax-3 molecules binding to the coverslip in both chambers were detected and measured using ImageJ plugin DoM_Utrecht v.0.9.1 (https://github.com/ekatrukha/DoM_Utrecht). The fitted peak intensity values were used to build fluorescence intensity histograms, which were compared to the intensity of Fchitax-3 signal on microtubules. The histograms were fitted to Gaussian distributions using GraphPad Prism 7.

Analysis of EB3 intensity fluctuations at the microtubule plus end

The distributions of EB3 intensities (normalized to the maximum value) were analyzed during the course of a growth event in control conditions (15µM tubulin, 20nM EB3) or with the addition of 100nM Fchitax-3. In case of Fchitax-3, fluctuations of EB3 intensity were analyzed before the initiation of Fchitax-3 accumulation and during the course of Fchitax-3 accumulations. For control measurements, we excluded the EB3 signal during the last phase of growth before catastrophe (pre-catastrophe phase) from our analysis as at this point the comet intensity is reduced[21, 49].

Laser ablation of microtubules in vitro

Laser photoablation assay in which an individual microtubule is severed by a focused laser beam was performed on the TIRF microscope equipped with an ILas system (Roper Scientific France/PICT-IBiSA) and a 532nm Q-switched pulsed laser (Teem Photonics). In vitro microtubule dynamics assay was performed in the presence of GMPCPP stabilized microtubule seeds with 15µM tubulin supplemented with 3% rhodamine-tubulin, 20nM mCherry-EB3 without or with 100nM Fchitax-3.

Fluorescence recovery after photobleaching (FRAP) assay

FRAP assay in which a region of a microtubule is bleached by a focused laser beam was carried on the TIRF microscope equipped with an ILas system (Roper Scientific France/PICT-IBiSA). In vitro microtubule dynamics assay was performed in the presence of GMPCPP stabilized microtubule seeds with 15µM tubulin supplemented with 3% rhodamine-tubulin without (control) or with 100nM Fchitax-3. Photobleaching in the tubulin channel was performed with the 561nm laser. In case of control, a segment of GDP microtubule lattice was photobleached. In case of Fchitax-3 containing samples, photobleaching was performed in the microtubule segment with Fchitax-3 accumulation zone.

X-Ray fiber diffraction experiments

X-Ray fiber diffraction images were collected in beamline BL11-NCD-SWEET of ALBA Synchrotron. Purified bovine tubulin was diluted to a final concentration of 100µM of PEM buffer (80mM PIPES, 1mM EGTA, 0.2mM Tris, 1mM DTT, 3mM $MgCl_2$). GDP-tubulin was obtained from diluted tubulin by hydrolysis, by incubating diluted protein for 30min at 37ºC and then supplementing the samples with 1mM GDP. GTP-tubulin was obtained by supplementing

the dilution buffer with 2mM GTP. Microtubules were obtained incubating tubulin samples for 30min at 37ºC to achieve maximum polymerization. 200µM Taxol was added to the samples either before microtubule polymerization (pre-assembly assays) or after polymerization (post-assembly assays). The samples were then mixed at 1:1 volume ratio with pre-warmed PEM buffer containing 2% Methylcellulose (MO512, Sigma-Aldrich). Final concentrations of protein, nucleotide and compounds were 50µM tubulin, 100µM Taxol and 1mM GTP or 1mM GDP. Samples were centrifuged 10s at 2000g to eliminate air bubbles and transferred to a share flow device[50, 51].

For each condition, a total 24 of diffraction images were averaged and background subtracted using ImageJ software (version 1.51j8; Wayne Rasband, National Institutes of Health, Bethesda, USA). Angular image integrations were performed using XRTools software (obtained from beamline BM26-DUBBLE of the European Synchrotron Radiation Facility (ESRF)). For average monomer length determination, 4th harmonic of the first layer line signals (1nm peak, 4th layer line) was fitted to a single-peaked Lorentzian function using Sigma-Plot software (Version 12.0) using peak maxima distance to center to calculate average monomer length.

Averaging of EB3 and Fchitax-3 intensity time traces

Simultaneous two color imaging of Fchitax-3/mCherry-EB3 was performed using an OptoSplit III beamsplitter (Cairn Research Ltd, UK) equipped with double emission filter cube projecting two channels on the camera chip simultaneously. Cromatic aberrations were corrected as described previously using calibration photomask[47]. Registered videos were used to create kymographs by drawing segmented lines of 10 pixel width (0.65µm) along growing microtubules using KymoResliceWide plugin with maximum transverse intensity (http://fiji.sc/KymoResliceWide). On extracted kymographs, we outlined rectangular ROI around

828 observed accumulation event and exported both intensities. For each frame, we fitted mCherry-
829 EB3 profile with sum of constant (lattice binding) and exponential decay functions (comet)
830 convoluted with microscope's PSF:

$$I(x,t) = I_{BG} + \frac{1}{2} I_{lattice} \cdot \mathrm{erfc}\left(\frac{x - x_c}{\sqrt{2}\sigma}\right) +$$

831 $$+ \frac{1}{2} I_{peak} \cdot \exp\left(\frac{\lambda}{2}\left(\sigma^2\lambda + 2(x - x_c)\right)\right) \cdot \left(1 - \mathrm{erf}\left(\frac{\sigma^2\lambda + x - x_c}{\sqrt{2}\sigma}\right)\right) \quad (1)$$

832 where fitting parameter I_{BG} corresponds to the intensity of background, $I_{lattice}$ to the amplitude of
833 the fluorescent intensity fraction associated with the lattice binding, I_{peak} to the amplitude of
834 convolved exponential decay, x_c to the position of the maximum number of molecules in the
835 molecules distribution (start of exponential decay position), σ to the PSF standard deviation and λ
836 to the exponential decay constant. From the fitted function $I(x,t)$ at each time frame t we obtained
837 maximum fluorescent intensity $I_{\mathrm{EB3}}(t) = \max_x I(x,t)$.
838 Intensity of Fchitax-3 was fitted with Gaussian function with background, where the width was a
839 fitting parameter. Total intensity was calculated as an integrated area under the fitted curve
840 (without background intensity) and provided $I_{\mathrm{Fchitax\text{-}3}}(t)$. This function for each kymograph was
841 further fitted with dose-response Hill equation, substituting the concentration for time:

842 $$I_{Fchitax-3}(t) = I_{BG} + \frac{I_{Max} - I_{BG}}{1 + \left(\frac{\tau_{50\%}}{t}\right)^h} \quad (2)$$

843 where fitting parameter I_{BG} corresponds to the background fluorescence, I_{Max} is maximum
844 intensity of Fchitax-3, h is a Hill coefficient and $\tau_{50\%}$ corresponds to the time when intensity
845 reaches half of its value. The choice of Hill equation was just a matter of convenience, other
846 sigmoid-like functions (for example, error function) worked equally well. All $I_{\mathrm{EB3}}(t)$ and $I_{\mathrm{Fchitax\text{-}3}}(t)$
847 intensity traces were normalized by the minimum and maximum values and shifted in a way

that $\tau_{50\%}$ moments were aligned (making this point t=0). For the averaging at the same time-sampling moments intensity profiles were linearly interpolated with the step of 0.1 of a frame.

Analysis of microtubule fluctuations

To estimate the transversal fluctuations of the microtubule tip, before, during and after the Fchitax-3 accumulation, we first determined the position of the microtubule tip. The tracking of microtubule plus-ends was performed using Trackmate plugin in Fiji (http://fiji.sc/TrackMate)[52]. Post-processing of the tracks was carried out by a custom made script in MATLAB. For each growth event, the tracking provided coordinates $x(t_i)$ and $y(t_i)$ of the fluorescent peak of an EB3 comet in the plane of the coverslip over time points $t_i, i \in [1,...,N]$. The trajectory of the comet was fit with a straight line $y = mx + c$ (forced to pass through x_S and y_S) to find the average axis of microtubule growth. To split the movement of the microtubule end into longitudinal $x_r(t)$ and transverse $y_r(t)$ components, we moved the origin of coordinates to the plus-end of the microtubule seed and rotated the xy plane to align the microtubule growth axis with the x-axis using the transform:

$$\begin{bmatrix} x_r \\ y_r \end{bmatrix} = \begin{bmatrix} \cos\theta & -\sin\theta \\ \sin\theta & \cos\theta \end{bmatrix} \begin{bmatrix} x - x_S \\ y - y_S \end{bmatrix} \tag{3}$$

where the value of rotation angle θ is equal to $\arctan(m)$. The characteristic standard deviation of the transverse deflection was calculated as

$$\sigma_y = \sqrt{\frac{1}{N-1} \sum_{i=1}^{N} (y_r(t_i) - \overline{y_r})} \tag{4}$$

where y_r is the average deflection per track.

Cryo-EM

For sample preparation, microtubules were polymerized from GMPCPP seeds with 1mM GTP, 15µM Tubulin, 20nM mCherry-EB3 and in the absence or presence of 100nM Fchitax-3 at 37℃ for 10min (designated -Fchitax-3 and +Fchitax-3 sample respectively). 4µl of each sample was applied to holey carbon grids (C-flat 2/2, Protochips) glow-discharged in air, before blotting and plunge-freezing using Vitrobot Mark IV (Thermo Fisher Scientific) at 22℃ and 100% humidity.

All cryo-EM micrographs were collected using a Tecnai T12 transmission electron microscope (Thermo Fisher) with a 4*4K CCD camera (Gatan) at 120kV, magnification of 52000, image pixel size of 2.09Å and defocus around -5µm.

For microtubule defect analysis, images from the -Fchitax-3 and +Fchitax-3 datasets collected by one team member were randomly mixed and were scored blindly by another team member for the presence/absence of small lattice defects (< ~40nm) and larger, sheet-like lattice defects (> ~40nm). Only microtubules that were longer than half a frame width and were not squashed by adjacent microtubules were included in the analysis. Following scoring, the frequency data were regrouped according to polymerization condition and differences between ±Fchitax-3 microtubules were evaluated for statistical significance using Pearson's chi-square test using GraphPad Prism 7.

Statistical analysis

All the histograms were plotted in GraphPad Prism 7, and statistical analysis was done using non-parametric Mann-Whitney U-test. For figure 6c, one sided Pearson's chi-square test was performed. All reported experiments were performed 2 or more times independently.

Kinetic model of Fchitax-3 accumulation

To understand how the observed dynamics of Fchitax-3 accumulation can emerge from the underlying molecular interactions, we generated a set of kinetic models based on our imaging data. Comparison of models with experimental data allowed us to eliminate contradicting mechanisms and narrow down the set to a single model presented at Fig. 4B. Below, we describe considered models and their underlying assumptions.

First of all, Fchitax-3 does not bind to microtubule lattice continuously, and its accumulation occurs only at specific moments during microtubule growth. Therefore, we assumed that at some time point, a special tubulin state [$Tu^{receptive}$] becomes accessible at the tip of a growing microtubule. This tubulin state can bind Fchitax-3 molecules leading to formation of [$Tu^{receptive}$·Fchitax3] complex, observed in experiments. Since after the initial accumulation the intensity of Fchitax-3 at microtubule irreversibly decline (Fig. 4a), we postulated that there is a transition from Fchitax-3 bound tubulin state to another state [$Tu^{lattice}$], that is unable to bind Fchitax-3 (accompanied by release of Fchitax-3). This transition can be attributed to the overall structural rearrangement of microtubule lattice. The described kinetic scheme is equivalent to the Michaelis-Menten model[53] (denoted here M1), where tubulin is considered as a substrate and Fchitax-3 as an enzyme. Assuming Fchitax-3 concentration in solution remains constant, the corresponding kinetic equations are:

$$\frac{dx(t)}{dt} = -k_1[\text{Fchitax3}]x + k_{-1}y, \qquad \text{(M1.1)} \qquad (5)$$

$$\frac{dy(t)}{dt} = k_1[\text{Fchitax3}]x - k_{-1}y - k_3y, \qquad \text{(M1.2)} \qquad (6)$$

$$x(0) = \left[\text{Tu}^{\text{receptive}}\right]_0,\ y(0) = 0;$$

$$x(t) = \left[\text{Tu}^{\text{receptive}}\right](t),\ y(t) = \left[\text{Tu}^{\text{receptive}} \cdot \text{Fchitax3}\right](t). \qquad \text{(M1.3)} \qquad (7)$$

where $x(t)$ corresponds to the concentration of [$Tu^{receptive}$] tubulin state, $y(t)$ to its complex with Fchitax-3 [$Tu^{receptive}$·Fchitax-3], k_1 and k_{-1} are rate constants of Fchitax-3 binding and unbinding and k_3 is the rate constant of transition to [$Tu^{lattice}$] state. We assumed that at the initial moment, there is no [$Tu^{receptive}$·Fchitax-3] complex present and there is some fixed number of [$Tu^{receptive}$] binding sites.

To fit model (M1.1-3) to experimental data, we built a kymograph of accumulation using KymoResliceWide plugin v.0.5 for Fiji [https://github.com/ekatrukha/KymoResliceWide] using the "maximum intensity transverse to line" option. We subtracted background intensity from the kymograph of Fchitax-3 and normalized it by maximum intensity value (after background subtraction). In this way, the maximum number of Fchitax-3 molecules per pixel over the whole duration of accumulation is equal to one. We built Fchitax-3 intensity traces over time at each pixel position along microtubule zones with Fchitax-3 accumulation. To estimate the initial moment of accumulation at specific position along the microtubule, we fitted the initial phase of Fchitax-3 increasing intensity with dose-response Hill equation, substituting the concentration for time:

$$I_{Fchitax3}(t) = I_{BG} + \frac{I_{Max} - I_{BG}}{1 + \left(\frac{\tau_{50\%}}{t}\right)^h} \quad (8)$$

where fitting parameter I_{BG} corresponds to the background fluorescence, I_{Max} is maximum intensity of Fchitax-3, h is a Hill coefficient and $\tau_{50\%}$ corresponds to the time when the intensity reaches half of its value. The choice of the Hill equation was just a matter of convenience, other sigmoid-like functions (for example, error function) worked equally well. The fitting was performed in MATLAB (2011b, The MathWorks, Inc, MA, USA). We estimated the initial moment of accumulation as $\tau_{3\%}$:

937 $$\tau_{3\%} = \tau_{50\%}\left(\frac{3\%}{100\%-3\%}\right)^{1/h} \quad (9)$$

938 Choosing any other value between 1% or 3% didn't change the outcome of the analysis. At each
939 pixel of accumulation along a microtubule, the normalized Fchitax-3 intensity from the moment
940 of $\tau_{3\%}$ until the end of the acquisition was used as an input to fit a kinetic model. Analytical
941 solution of the model (M1.1-3) was found using Mathematica v.11.0.1.0 (Wolfram Research,
942 Champaign, IL, USA). The derived function $y(t)$, i.e. the solution of M1.2 and M1.3 was fitted to
943 the Fchitax-3 intensity time trace with *NonlinearModelFit* function using rate constants and
944 initial concentration values as fitting parameters.

945

946 The final best fit of Michaelis-Menten model (see Fig. 4c for a representative example) did not
947 provide a satisfying description of the shape of the kinetic curve. This discrepancy can be
948 attributed to the fact that simple binding-unbinding kinetics (M1.1) cannot produce the observed
949 rapid increase in the accumulation of Fchitax-3 and required the addition of a non-linearity. To
950 overcome this, we introduced a simple autocatalysis/cooperativity step, where the presence of
951 [$\mathrm{Tu}^{\mathrm{receptive}}$·Fchitax-3] complex increases the probability of Fchitax-3 binding to [$\mathrm{Tu}^{\mathrm{receptive}}$] tubulin
952 (see Supplementary Fig. 5B). Modified kinetic equations are:

953

954 $$\frac{dx(t)}{dt} = -k_1[\mathrm{Fchitax3}]x + k_{-1}y - k_2xy, \quad \text{(M2.1)} \quad (10)$$

955 $$\frac{dy(t)}{dt} = k_1[\mathrm{Fchitax3}]x - k_{-1}y + k_2xy - k_3y, \quad \text{(M2.2)} \quad (11)$$

956 $$x(0) = \left[\mathrm{Tu}^{\mathrm{receptive}}\right]_0,\ y(0) = 0;$$

957 $$x(t) = \left[\mathrm{Tu}^{\mathrm{receptive}}\right](t),\ y(t) = \left[\mathrm{Tu}^{\mathrm{receptive}} \cdot \mathrm{Fchitax3}\right](t). \quad \text{(M2.3)} \quad (12)$$

958

959 where k_2 corresponds to the rate constant of the autocatalysis. Since this system of differential
960 equations (M2.1-3) cannot be solved analytically, it was solved numerically, using
961 *ParametricNDSolveValue* function of Mathematica. The same function and workflow were also
962 used for the other non-linear models described below in this section. Residuals between the
963 solution and experimental data were minimized using *NonlinearModelFit* function with
964 Levenberg-Marquardt optimizer. Due to physical constrains on parameters values (i.e. rate
965 constants values should be always positive), the optimizer not always converged to a true
966 minimum in the parameter space, sometimes stalling at the borders. In this case, the relative
967 fitting errors of parameters exceeded 100%. For such fits another set of initial parameters for the
968 optimizer was chosen. If the minimum was still not found, the fit was discarded.
969
970 The model 2 (M2) provided much better fit to the experimentally observed kinetic curve
971 (Supplementary Fig. 5c,e) confirming that the addition of an autocatalysis step is necessary to
972 explain the experimental data. However, this model yielded values of dissociation constant k_{-1} in
973 the range of 0.2 - 0.5s^{-1}, one order of magnitude higher than the values estimated from FRAP
974 experiments (Fig. 5d). Simulated FRAP experiments show that Fchitax-3 recovery is almost
975 immediate, contradicting experimental data (Fig. 4e and Supplementary Fig. 5f). This can be
976 explained by the fact that the dissociation rate in this case has to compensate for the much faster
977 Fchitax-3 association, which is self-accelerated due to autocatalysis. Therefore, we excluded this
978 kinetic mechanism.
979
980 In both models described above, it was assumed that an Fchitax-3 accumulation starts with a
981 sudden appearance of substantial amount of [$Tu^{receptive}$] tubulin state (GMPCPP-like) at the tip of
982 growing microtubule (Supplementary Fig. 5e). Instantaneous emergence of such structure seemed

983 implausible. Therefore, we considered an alternative scenario, where the majority of tubulin
984 molecules exist in some initial state [$Tu^{unreceptive}$] that is unable to bind Fchitax-3. If a small
985 number of [$Tu^{receptive}$] tubulins appears, this leads to [$Tu^{receptive}$·Fchitax-3] complex formation that
986 can catalyze the transition of additional [$Tu^{unreceptive}$] tubulin molecules to the [$Tu^{receptive}$] state.
987 The corresponding kinetic equations are:
988

989 $$\frac{dx(t)}{dt} = -k_1[\text{Fchitax3}]x + k_{-1}y, \quad \text{(M3.1)} \quad (13)$$

990 $$\frac{dy(t)}{dt} = k_1[\text{Fchitax3}]x - k_{-1}y + k_2zy - k_3y, \quad \text{(M3.2)} \quad (14)$$

991 $$\frac{dz(t)}{dt} = -k_2zy, \quad \text{(M3.3)} \quad (15)$$

$$x(0) = \left[\text{Tu}^{\text{receptive}}\right]_0;\ \ y(0) = 0;\ \ z(0) = \left[\text{Tu}^{\text{unreceptive}}\right]_0,$$

992 $$x(t) = \left[\text{Tu}^{\text{receptive}}\right](t),\ y(t) = \left[\text{Tu}^{\text{receptive}} \cdot \text{Fchitax3}\right](t), z(t) = \left[\text{Tu}^{\text{unreceptive}}\right](t). \quad \text{(M3.4)} \ (16)$$

993 where $z(t)$ corresponds to the concentration of [$Tu^{unreceptive}$] tubulin state and k_2 is the rate
994 constant of autocatalysis. The numerical solution of the (M3.1-4) model is highly unstable, but
995 nevertheless the best obtained fits provided poor description of experimental data (Supplementary
996 Fig. 5c). In addition, the values of dissociation constant k_{-1} were in the same range as in model
997 (M2.1-3), contradicting our FRAP data.
998

999 After considering different kinetic schemes, we found that a model where the Fchitax-3 binding
1000 to [$Tu^{receptive}$] itself catalyzes transformation of another (possibly neighboring) [$Tu^{unreceptive}$] to
1001 [$Tu^{receptive}$] state, describes experimental data best. The corresponding system of kinetic equations
1002 is:
1003

1004 $\frac{dx(t)}{dt} = -k_1[\text{Fchitax3}]x + k_{-1}y,$ (M4.1) (17)

1005 $\frac{dy(t)}{dt} = k_1[\text{Fchitax3}]x - k_{-1}y + k_2zx - k_3y,$ (M4.2) (18)

1006 $\frac{dz(t)}{dt} = -k_2zx,$ (M4.3) (19)

$$x(0) = \left[\text{Tu}^{\text{receptive}}\right]_0;\ \ y(0) = 0;\ \ z(0) = \left[\text{Tu}^{\text{unreceptive}}\right]_0,$$

1007 $x(t) = \left[\text{Tu}^{\text{receptive}}\right](t),\ y(t) = \left[\text{Tu}^{\text{receptive}} \cdot Fchitax3\right](t), z(t) = \left[\text{Tu}^{\text{unreceptive}}\right](t).$ (M4.4)

1008 (20)

1009

1010 The final best fits of the model (M4.1-4) together with FRAP simulations are presented at Fig.
1011 4c,f. The solutions for kinetics of [$\text{Tu}^{\text{unreceptive}}$], [$\text{Tu}^{\text{receptive}}$] and [$\text{Tu}^{\text{receptive}}$ ·Fchitax-3] for a
1012 representative fit are shown at Supplementary Fig. 5g. To calculate kinetics of FRAP, first we
1013 solved equations (M4.1-4) till the moment of bleaching t_{FRAP}. After that, we considered the
1014 following system:

1015

1016 $\frac{d\tilde{x}(t)}{dt} = -k_1[\text{Fchitax3}]\tilde{x} + k_{-1}\tilde{y} + k_{-1}y_{bleached},$ (M4F.1) (21)

1017 $\frac{d\tilde{y}(t)}{dt} = k_1[\text{Fchitax3}]\tilde{x} - k_{-1}\tilde{y} + k_2\tilde{z}\tilde{x} - k_3\tilde{y},$ (M4F.2) (22)

1018 $\frac{d\tilde{z}(t)}{dt} = -k_2\tilde{z}\tilde{x},$ (M4F.3) (23)

1019 $\frac{dy_{bleached}(t)}{dt} = -k_{-1}y_{bleached} - k_3y_{bleached},$ (M4F.4) (24)

1020 $\tilde{x}(0) = x(t_{FRAP});\ \ y_{bleached}(0) = y(t_{FRAP});\ \tilde{z}(0) = z(t_{FRAP});\ \ \tilde{y}(0) = 0;$ (M4F.5) (25)

1021 where $y_{bleached}(t)$ corresponds to the concentration of the photobleached molecules of [$\text{Tu}^{\text{receptive}}$
1022 ·Fchitax-3] complex after the time t_{FRAP} and $\tilde{y}(t)$ are the newly absorbed molecules.

1023

For the long accumulation event presented at Fig. 4a we explored the dependence of model parameters on the position along an accumulation. Rate constants k_1, k_{-1} and k_3 slightly fluctuated around their average values and didn't show any significant trends. In contrast, the initial concentrations of [$Tu^{unreceptive}$] and [$Tu^{unreceptive}$] monotonically declined from the position at the beginning of accumulation towards its end (Supplementary Fig. 5d). This means that the size of structure on the microtubule lattice that interacts with Fchitax-3 is gradually decreasing, which might be attributed to the structural "closure" of microtubule lattice.

Data availability

All data that support the conclusions are available from the authors on request.

Code availability

All MATLAB and Mathematica notebooks used for computations, together with the raw data are available online [https://doi.org/10.6084/m9.figshare.7520033] and https://github.com/RuddiRodriguez/Analysis-of-MT-plus-end-fluctuations

References

46. Diaz, J.F. & Andreu, J.M. Assembly of purified GDP-tubulin into microtubules induced by taxol and taxotere: reversibility, ligand stoichiometry, and competition. *Biochemistry* **32**, 2747-2755 (1993).
47. Aher, A. *et al.* CLASP Suppresses Microtubule Catastrophes through a Single TOG Domain. *Dev Cell* **46**, 40-58 e48 (2018).

48. Gell, C. *et al.* Microtubule dynamics reconstituted in vitro and imaged by single-molecule fluorescence microscopy. *Methods Cell Biol* **95**, 221-245 (2010).

49. Maurer, S.P., Fourniol, F.J., Bohner, G., Moores, C.A. & Surrey, T. EBs recognize a nucleotide-dependent structural cap at growing microtubule ends. *Cell* **149**, 371-382 (2012).

50. Sugiyama, T. *et al.* Quick shear-flow alignment of biological filaments for X-ray fiber diffraction facilitated by methylcellulose. *Biophys J* **97**, 3132-3138 (2009).

51. Kamimura, S., Fujita, Y., Wada, Y., Yagi, T. & Iwamoto, H. X-ray fiber diffraction analysis shows dynamic changes in axial tubulin repeats in native microtubules depending on paclitaxel content, temperature and GTP-hydrolysis. *Cytoskeleton (Hoboken)* **73**, 131-144 (2016).

52. Tinevez, J.Y. *et al.* TrackMate: An open and extensible platform for single-particle tracking. *Methods* **115**, 80-90 (2017).

53. Michaelis, L., Menten, M.L., Johnson, K.A. & Goody, R.S. The original Michaelis constant: translation of the 1913 Michaelis-Menten paper. *Biochemistry* **50**, 8264-8269 (2011).

Figure 1: Rai et al.

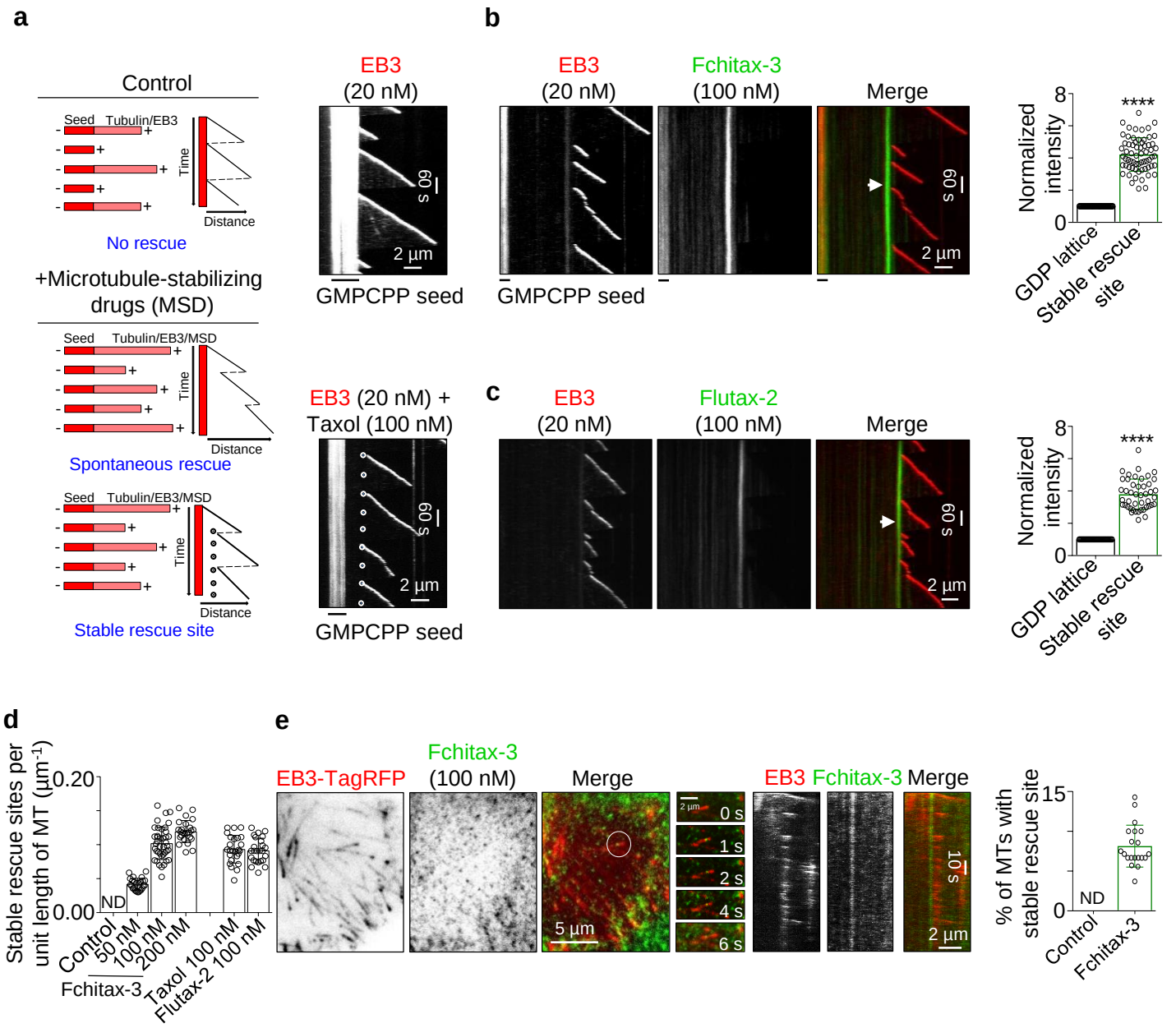

Figure 2: Rai et al.

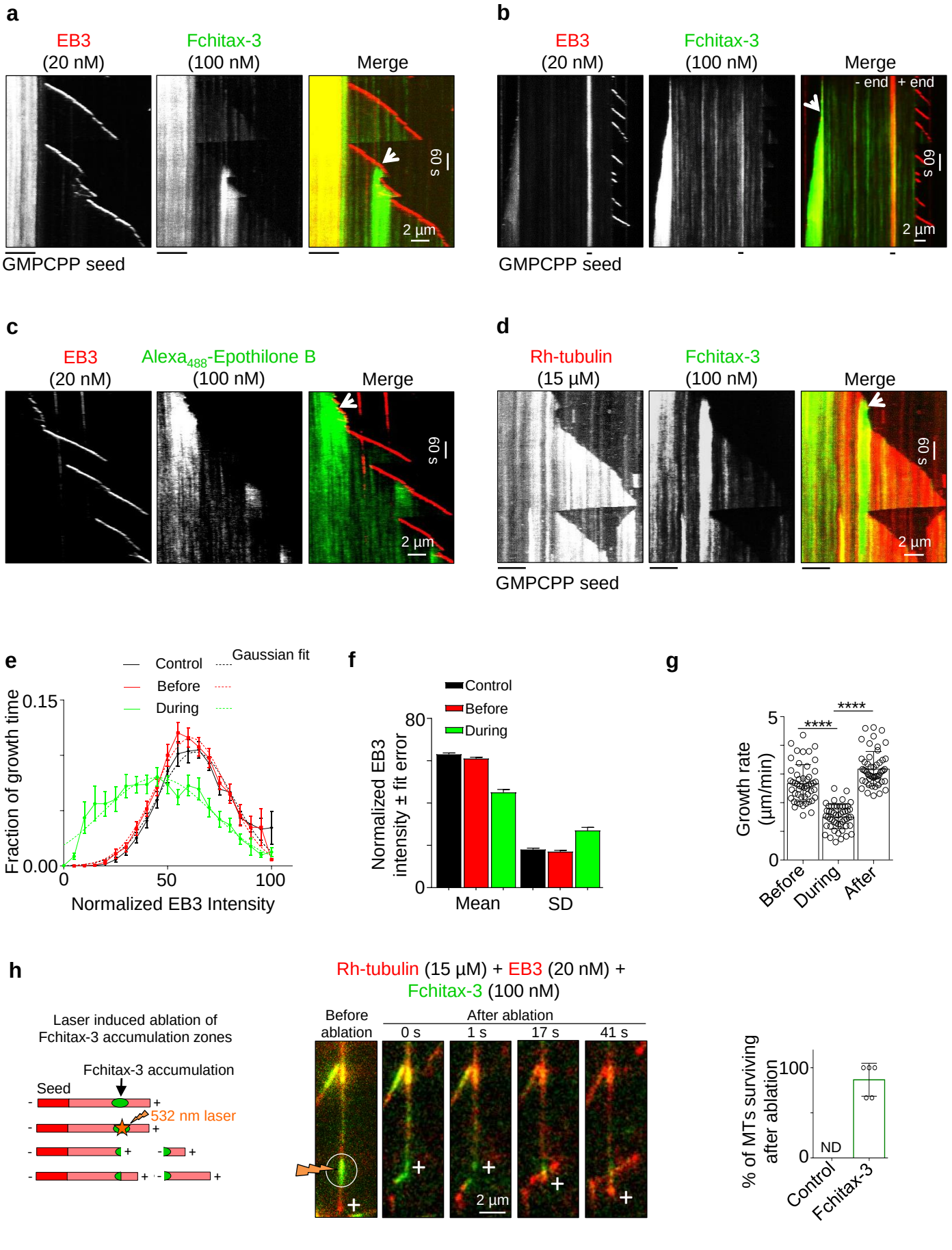

Figure 3: Rai et al.

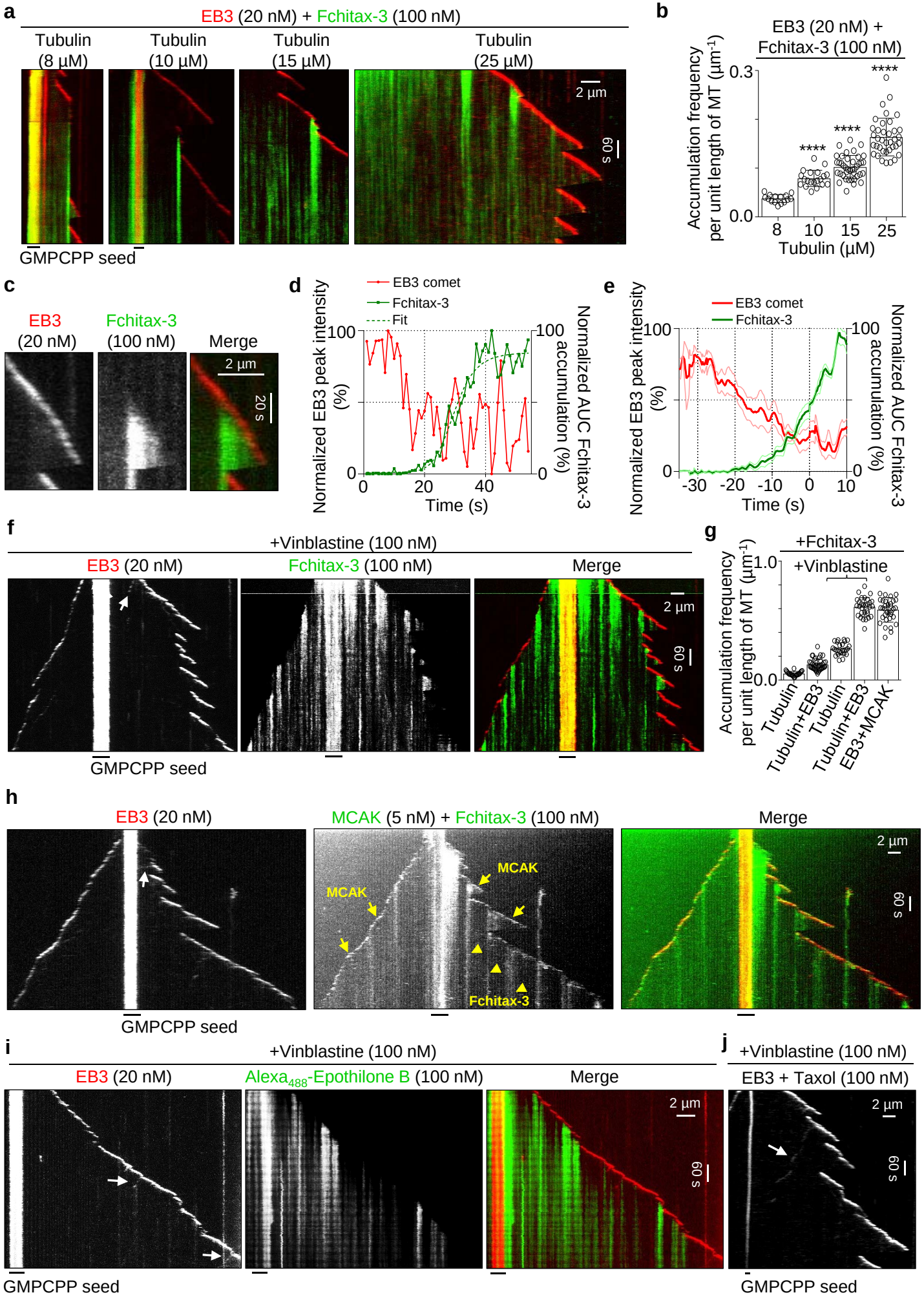

Figure 4: Rai et al.

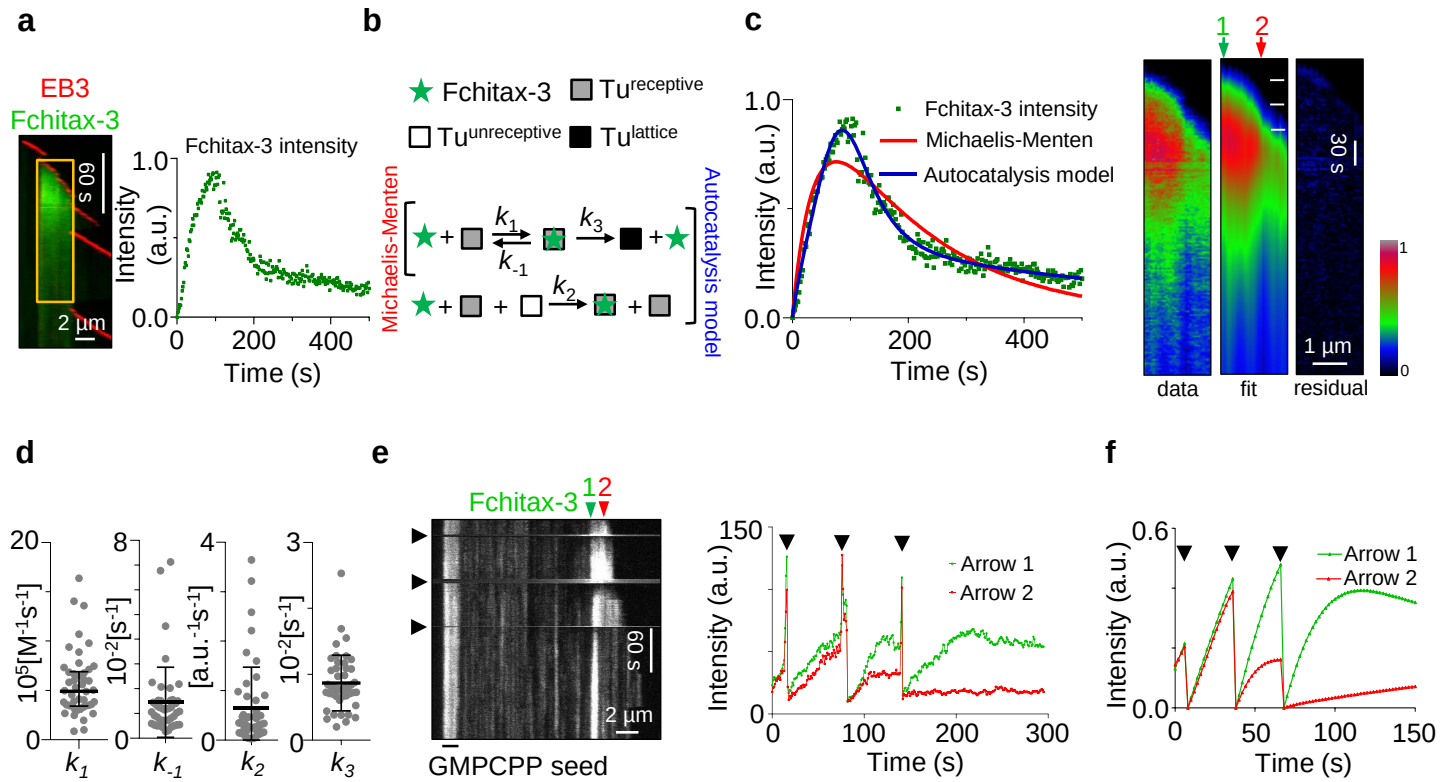

Figure 5: Rai et al.

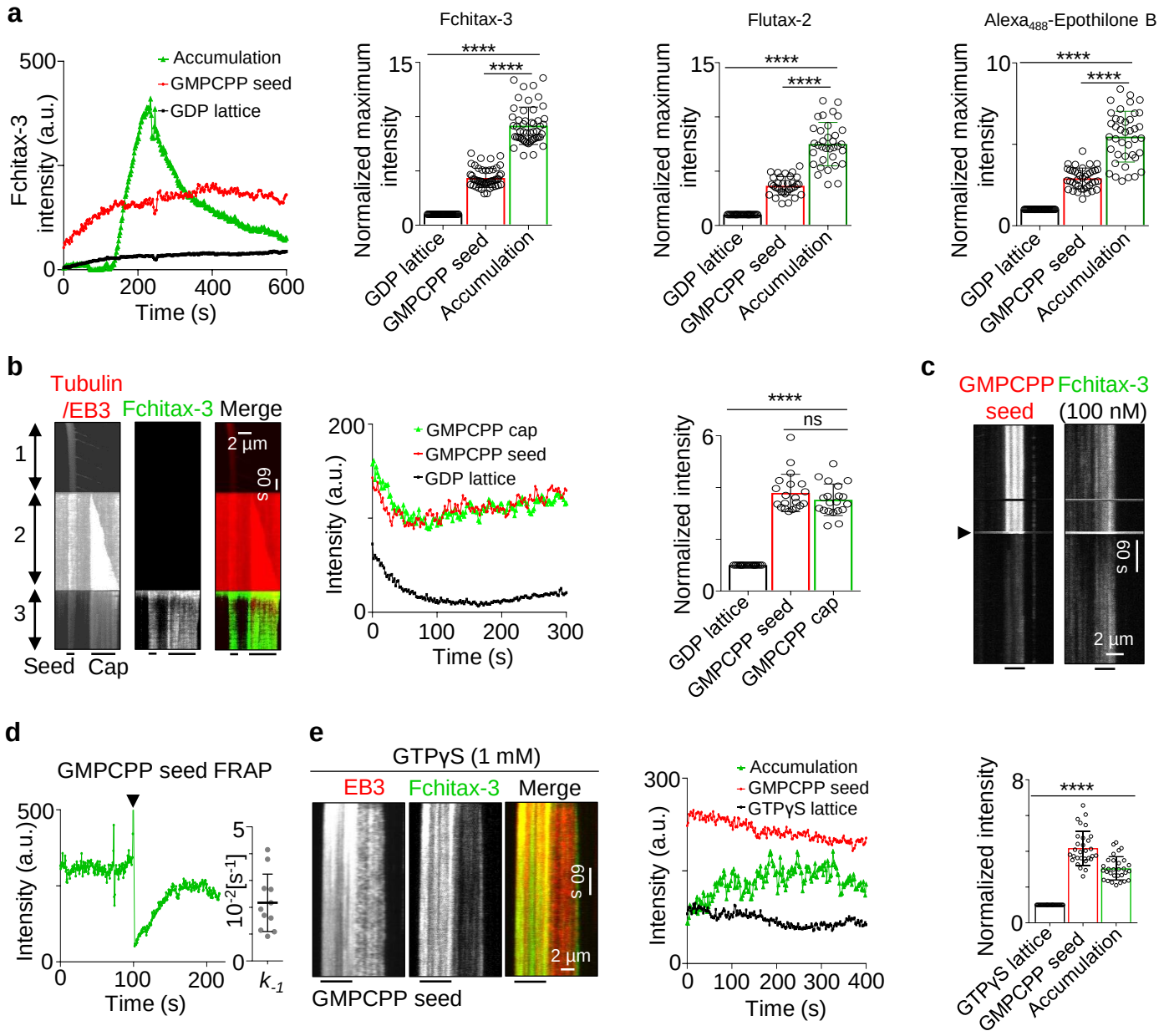

Figure 6: Rai et al.

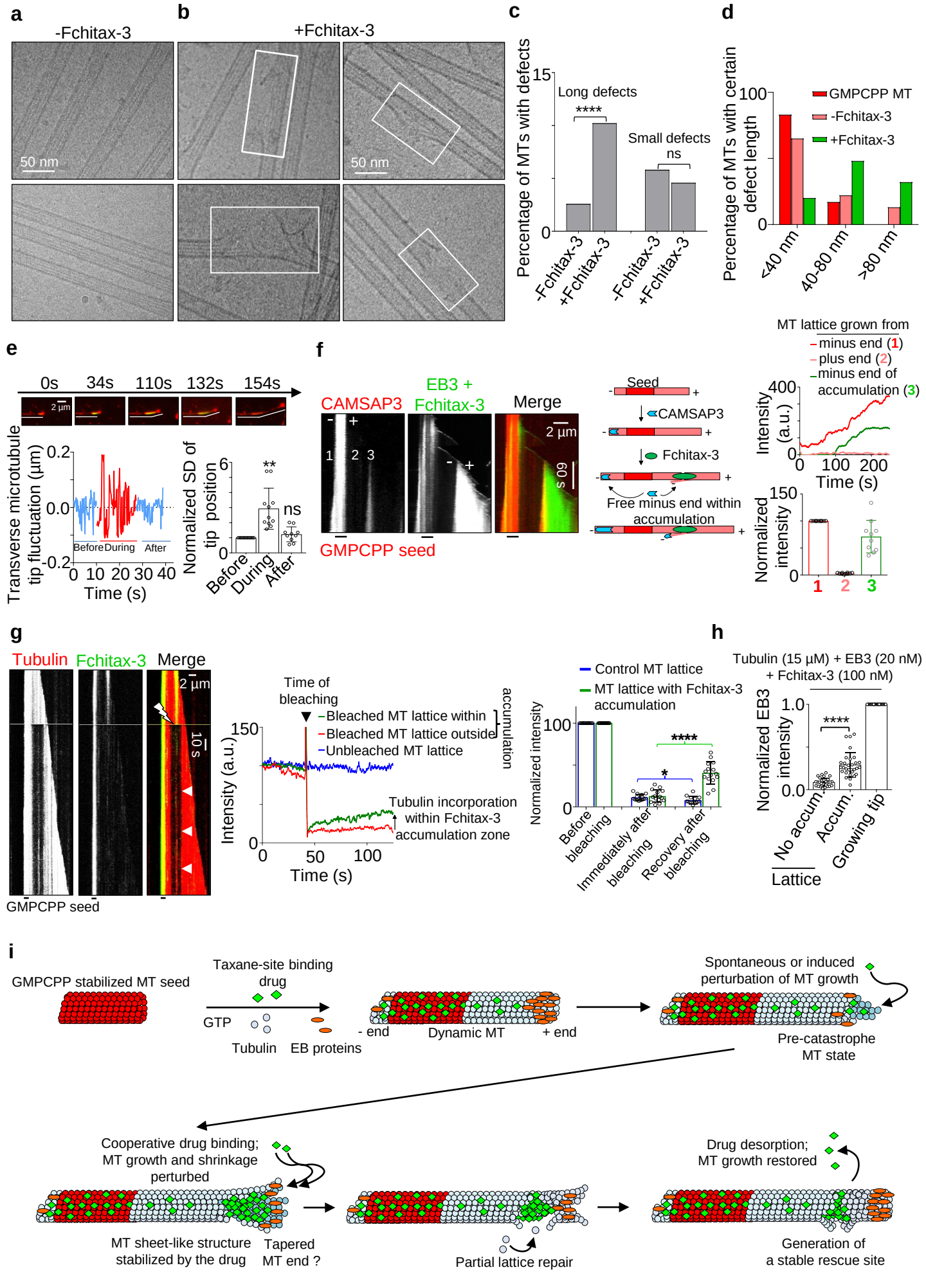

Supplementary Information for

Taxanes convert regions of perturbed microtubule growth into rescue sites

Ankit Rai[1], Tianyang Liu[2], Simon Glauser[3], Eugene A. Katrukha[1], Juan Estévez-Gallego[4], Ruddi Rodríguez-García[1], Wei-Shuo Fang[5], J. Fernando Díaz[4], Michel O. Steinmetz[6,7], Karl-Heinz Altmann[3], Lukas C. Kapitein[1], Carolyn A. Moores[2] and Anna Akhmanova[1]

[1] Cell Biology, Department of Biology, Faculty of Science, Utrecht University, Padualaan 8, 3584 CH Utrecht, the Netherlands

[2] Institute of Structural and Molecular Biology, Birkbeck, University of London, Malet Street, London, United Kingdom

[3] Department of Chemistry and Applied Biosciences, Institute of Pharmaceutical Sciences, ETH Zürich, 8092 Zürich, Switzerland.

[4] Chemical and Physical Biology, Centro de Investigaciones Biológicas, Consejo Superior de Investigaciones Científicas CIB-CSIC, Ramiro de Maeztu 9, 28040, Madrid, Spain

[5] State Key Laboratory of Bioactive Substances and Functions of Natural Medicines, Institute of Materia Medica, CAMS & PUMC, 2A Nan Wei Road, Beijing, 100050, China

[6] Laboratory of Biomolecular Research, Division of Biology and Chemistry, Paul Scherrer Institut, 5232 Villigen PSI

[7] University of Basel, Biozentrum, CH-4056 Basel, Switzerland

Corresponding author: Anna Akhmanova, a.akhmanova@uu.nl.

Supplementary Figure 1

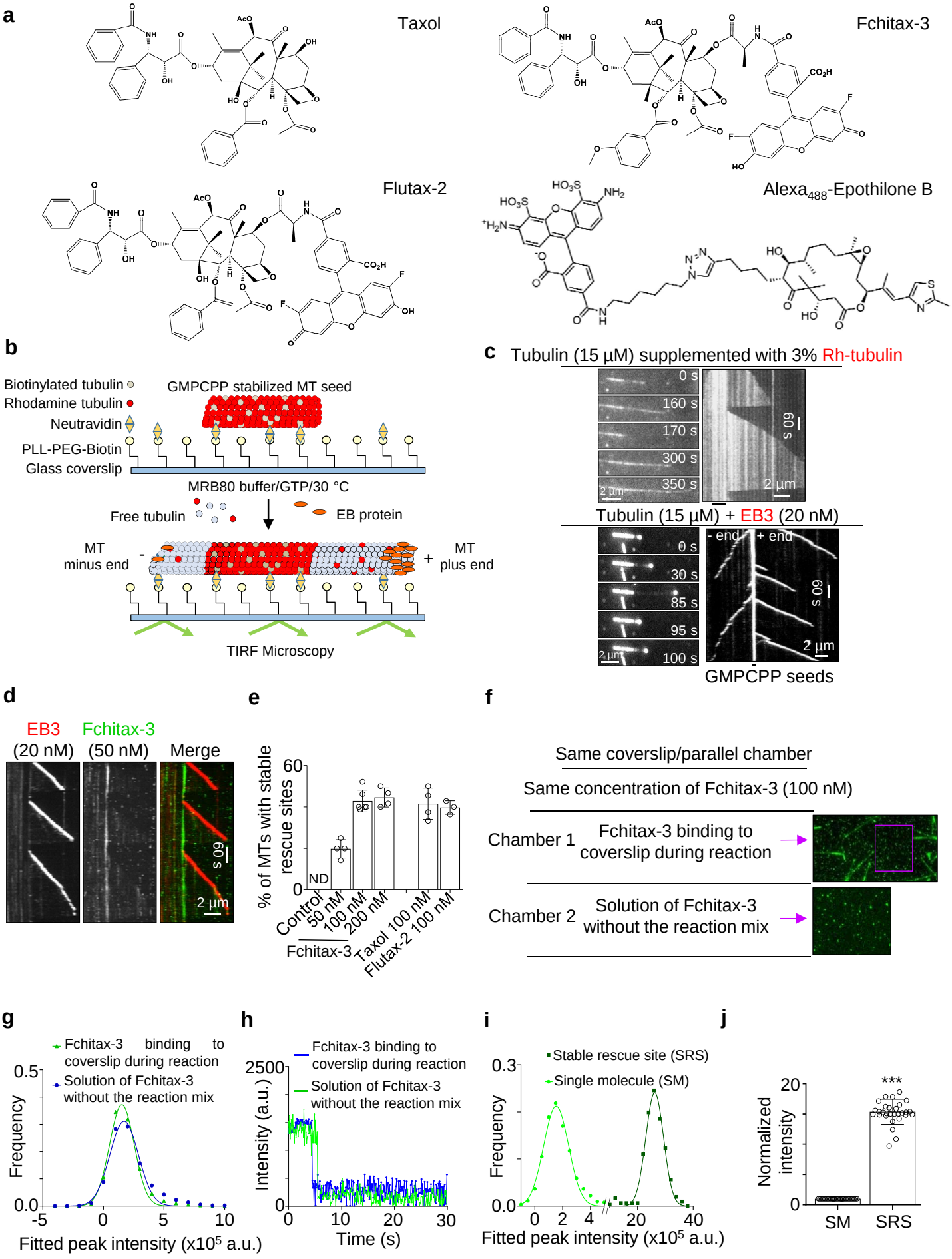

Supplementary Figure 1: Fluorescent compounds and microtubule dynamics assays

a) Structures of Taxol, Fchitax-3, Flutax-2 and Alexa$_{488}$-Epothilone B.

b) A scheme of the TIRF microscopy-based microtubule dynamics assay. GMPCPP-stabilized microtubule seeds that contain fluorescent tubulin such as rhodamine tubulin (for visualization) and biotinylated tubulin (for surface attachment via NeutrAvidin), are immobilized on a plasma-cleaned coverslip coated with biotinylated poly(L-lysine)-[g]-poly(ethylene glycol) (PLL-PEG-biotin) which is coupled with NeutrAvidin. Microtubule growth from GMPCPP-stabilized seeds is initiated by adding either tubulin supplemented with fluorescent tubulin, or by adding unlabeled tubulin and GFP/mCherry-tagged-EB3. Microtubule plus and minus ends are indicated.

c) Time-lapse images and representative kymographs illustrating microtubule growth from GMPCPP stabilized microtubule seeds in the presence of tubulin (15µM) supplemented with 3% rhodamine-labeled tubulin (upper panel) and in the presence of unlabeled tubulin (15µM) and mCherry-EB3 (20nM) (lower panel). Kymographs are representative of 5 independent experiments.

d) Kymograph illustrating a stable rescue site formed in the presence of 15µM tubulin, 20nM mCherry-EB3 and 50nM Fchitax-3. Kymographs are representative of 3 independent experiments.

e) Quantification (mean values) of the occurrence of stable rescue sites at the indicated compound concentrations. ND, not detected. n=100 for control (N=6), n=35 (N=4), 79 (N=6), 45 (N=4) for 50, 100 and 200nM of Fchitax-3, respectively, n=46 (N=4) and 28 (N=3) for Taxol and Flutax-2. Error bars represent SD.

f) Fluorescence intensity measurement of single molecule of Fchitax-3 in two parallel chambers made on the same coverslip. In one chamber, microtubule dynamics assay was performed in the presence of GMPCPP stabilized microtubule seeds with 15µM tubulin, 20nM mCherry-EB3 and

100nM Fchitax-3. The intensity of Fchitax-3 molecules bound to coverslip was analysed in a microtubule-free region (purple square in the upper panel). The other chamber was incubated with the same concentration of Fchitax-3 without the reaction mix (lower panel). Images are representative of 3 independent experiments

g, h) Fluorescence intensities (g) and photobleaching time traces (h) of Fchitax-3 molecules immobilized on coverslips in solution of 100nM Fchitax-3 without the reaction mix (n=3546) or Fchitax-3 bound to coverslip during the microtubule dynamics assay (n=2014) in a separate chamber on the same coverslip. In (g), the measured values are shown by symbols, and the corresponding fits to Gaussian distributions by lines. For comparison, we used the intensity of Fchitax-3 molecules transiently immobilized on the same coverslip during the reaction. Such molecules had the same intensity and showed the same single-step photobleaching behavior as the Fchitax-3 molecules immobilized in a separate chamber on the same coverslip in the absence of any additional components.

i) Fluorescence intensities of single Fchitax-3 molecules bound to the coverslip during the reaction and of Fchitax-3 accumulations at stable rescue site (symbols); the corresponding fits to Gaussian distributions are shown with lines.

j) Fluorescence intensity (mean ± SD) of single Fchitax-3 molecules and the Fchitax-3 accumulations at dot-like stable rescue sites, normalized to single molecule intensity. n=30, N=4 independent experiments; error bar represents SD; ***p=0.0006, Mann–Whitney U-test.

Supplementary Figure 2

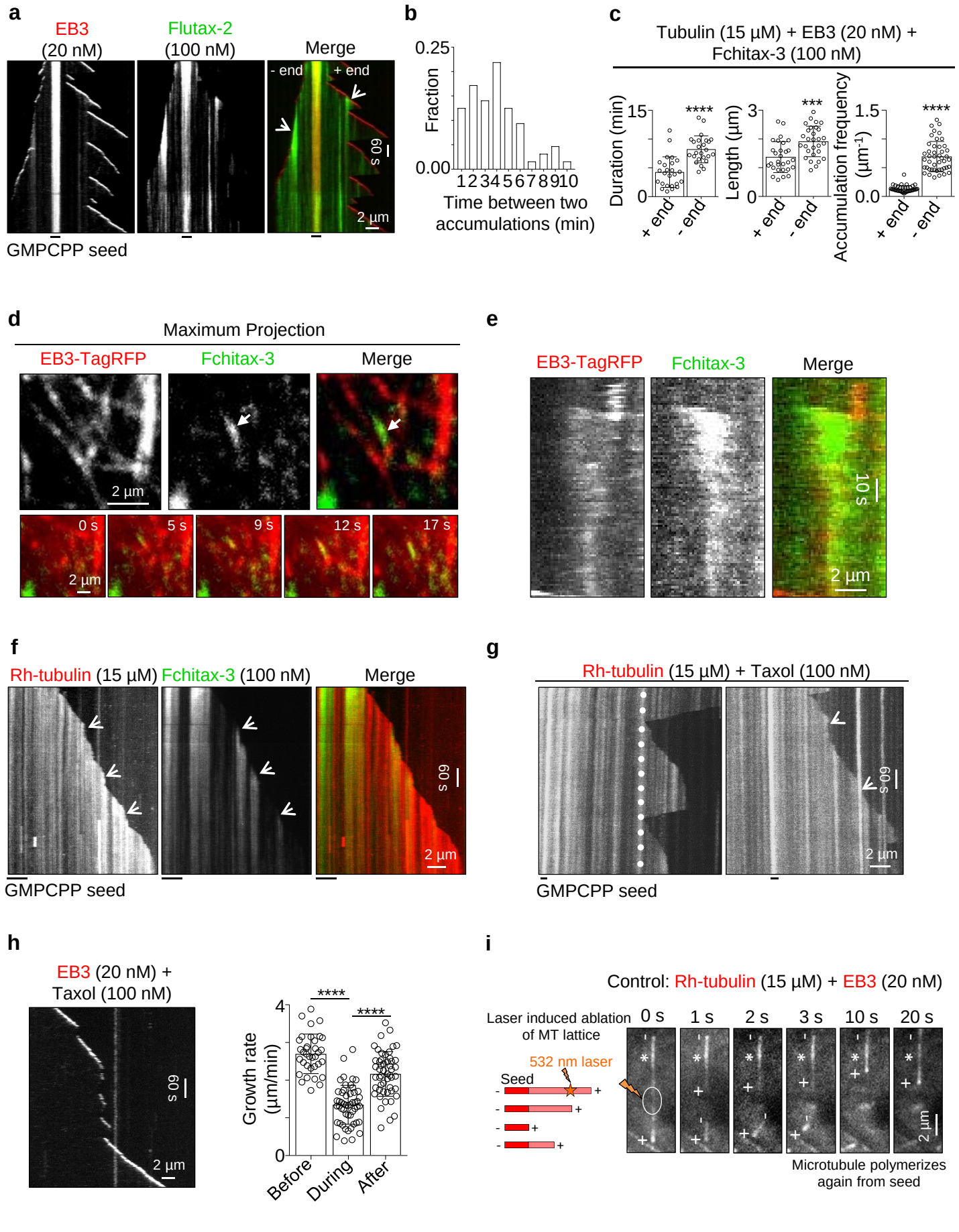

Supplementary Figure 2: Formation of taxane accumulations at growing microtubule ends.

a) Representative kymographs (N = 3 experiments) showing Flutax-2 accumulation at the plus- and the minus end of a microtubule (white arrows in the merge panel) in the presence of 15μM tubulin, 20nM mCherry-EB3 and 100nM Flutax-2.

b) Plot showing the analysis of the time interval between the appearances of two consecutive accumulations. 64 consecutive accumulation events from 5 independent experiments were analysed and relative frequencies of different interval durations were plotted.

c) Plots (mean values) showing quantification of the duration of Fchitax-3 accumulations (n=25, ****p <0.0001), length of Fchitax-3 accumulations (n=29, ***p <0.0003) and the frequency of Fchitax-3 accumulations, calculated per unit of microtubule length (n=40 for plus end and 45 for minus end, ****p <0.00001) at microtubule plus- and the minus ends. N=5 independent experiments, error bars represent SD, Mann–Whitney U-test.

d, e) Maximum projection (upper panels), time lapse images (lower panels) (d) and representative kymographs (e) illustrating an Fchitax-3 accumulation event (white arrows) in a HeLa cell transfected with EB3-TagRFP and incubated with 100nM Fchitax-3 for 1 hr. Images are representative of 2 independent experiments.

f) Representative kymographs (N = 3 experiments) illustrating perturbation of microtubule growth during Fchitax-3 accumulation events (white arrows in the tubulin and Fchitax-3 panels) in the presence of 15μM tubulin, supplemented with 3% rhodamine-tubulin, and 100nM Fchitax-3.

g) Representative kymographs (N = 2 experiments) illustrating a stable rescue site (highlighted by stippled white line) and perturbed microtubule growth (whites arrows) in the presence of 15μM tubulin, supplemented with 3% rhodamine-tubulin and 100 nM Taxol.

h) Kymograph illustrating microtubule growth perturbation in the presence of 15μM tubulin, 20nM mCherry-EB3 and 100nM Taxol. The right panel shows the quantification (mean values) of microtubule growth rate before (n=35), during (n=51) and after (n=51) the perturbed growth episode. N=3 independent experiment, Error bars represent SD, $p < 0.0001$, Mann–Whitney U-test.

i) A scheme and still images (representative of 3 independent experiments) illustrating laser ablation of a control microtubule in the presence of 15μM tubulin, supplemented with 3% rhodamine-tubulin and 20nM mCherry-EB3. The region of laser ablation is indicated by a lightning bolt and a white oval. The asterisks show the position of the GMPCPP seed. Microtubule plus- and minus ends are indicated.

Supplementary Figure 3

a

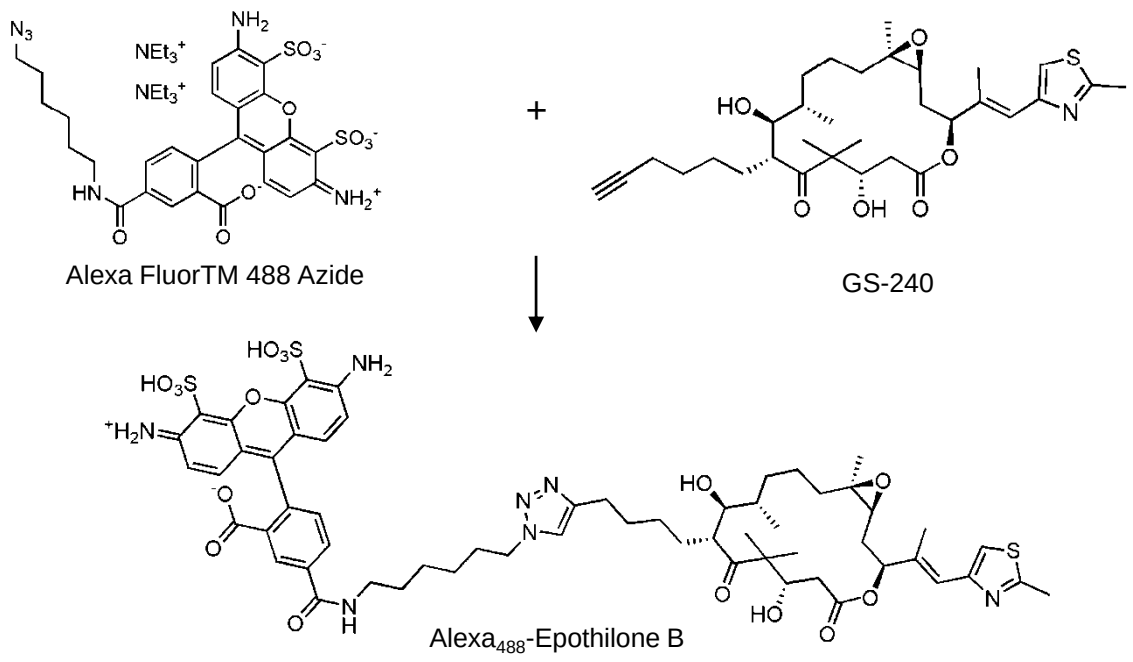

b

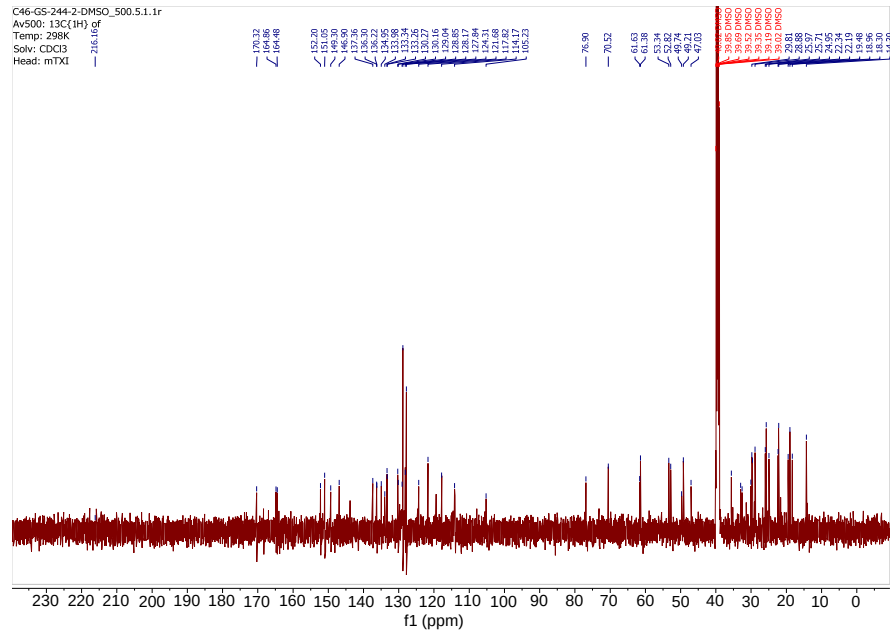

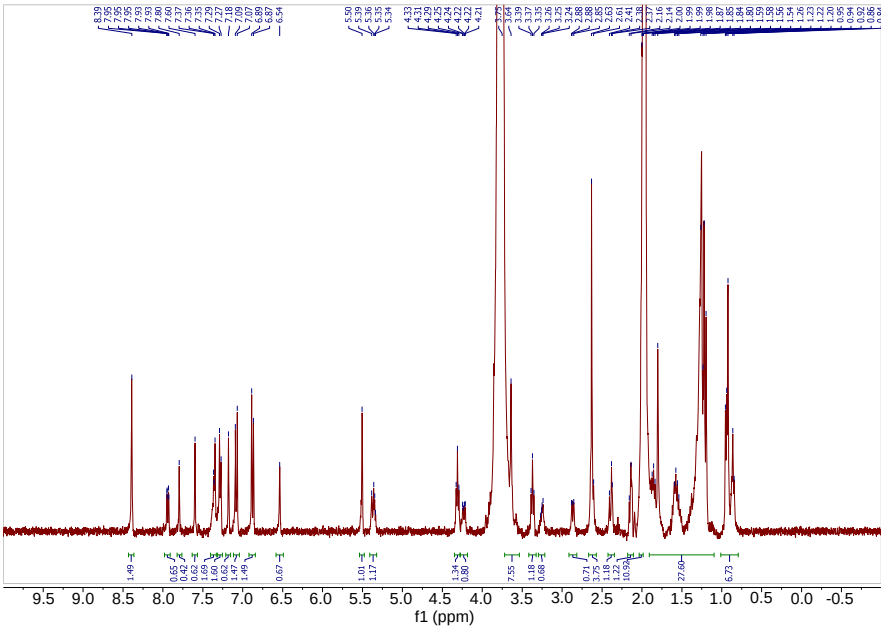

Supplementary Figure 3: Synthesis and characterization of Alexa$_{488}$-Epothilone B.

a**)** A scheme showing the reagents used for the synthesis of alexa-488 labelled epothilone B (see Methods for details).

b**)** Characterization of Alexa$_{488}$-Epothilone B by NMR spectroscopy.

^{1}H-NMR (400 MHz, Acetonitrile-d$_3$: D_2O (9:1)) δ 8.39 (s, 1H), 7.94 (dd, J = 8.1, 1.7 Hz, 1H), 7.80 (s, 1H), 7.60 (s, 1H), 7.40 – 7.32 (m, 1H), 7.28 (d, J = 7.8 Hz, 1H), 7.18 (s, 1H), 7.08 (d, J = 9.2 Hz, 1H), 6.88 (d, J = 9.3 Hz, 1H), 6.54 (s, 1H), 5.50 (s, 1H), 5.45 – 5.31 (m, 1H), 4.31 (t, J = 7.0 Hz, 1H), 4.27 – 4.18 (m, 1H), 3.64 (s, 3H), 3.37 (t, J = 7.1 Hz, 1H), 3.27 – 3.22 (m, 1H), 2.87 (d, J = 11.1 Hz, 1H), 2.63 (s, 3H), 2.42 – 2.36 (m, 1H), 2.15 (d, J = 9.5 Hz, 1H), 2.04 – 1.98 (m, 3H), 1.85 (s, 1H), 1.80 (s, 3H), 1.66 – 1.17 (m, >20H*), 1.00 –0.85 (m, >5H*). Due to the limited solubility of GS-244 across a range of solvents, no high quality spectrum could be recorded. Peaks labeled with an asterisk could not be assigned or integrated reliably.

^{13}C-NMR (126 MHz, DMSO-d$_6$) δ 216.16, 170.32, 164.86, 164.48, 152.20, 151.05, 149.30, 146.90, 137.36, 136.30, 136.22, 134.95, 133.98, 133.34, 133.26, 130.27, 130.16, 129.04, 128.85, 128.17, 127.84, 124.31, 121.68, 117.82, 114.17, 105.23, 76.90, 70.52, 61.63, 61.38, 53.34, 52.82, 49.74, 49.21, 47.03, 40.02, 39.85, 39.69, 39.52, 39.35, 39.19, 39.02, 35.61, 32.95, 32.58, 30.07, 29.81, 29.61, 28.88, 25.97, 25.71, 24.95, 22.34, 22.19, 19.48, 18.96, 18.30, 14.30. Due to the limited solubility of GS-244 across a range of solvents, no high quality spectrum could be recorded. The signals listed were cross-checked by HMBC and HSQC spectroscopy, but several quaternary carbons were not observable.

IR (film): ν3298, 2926, 2859, 1726, 1643, 1619, 1548, 1444, 1319, 1252, 1187, 1156, 1052.

$[\boldsymbol{\alpha}]_{\boldsymbol{D}}^{\mathbf{20}}$= -20.3° (c = 0.148 in MeCN: H_2O (1:1)).

HRMS (MALDI/ESI): calcd for $C_{59}H_{74}N_7O_{16}S_3$ [M^+H^+]: 1232.4349; found: 1232.4355.

The number of scans for the ^{13}C experiment is 32,000 and for the ^{1}H experiment was 256. The click reaction itself was performed 2 times.

Supplementary Figure 4

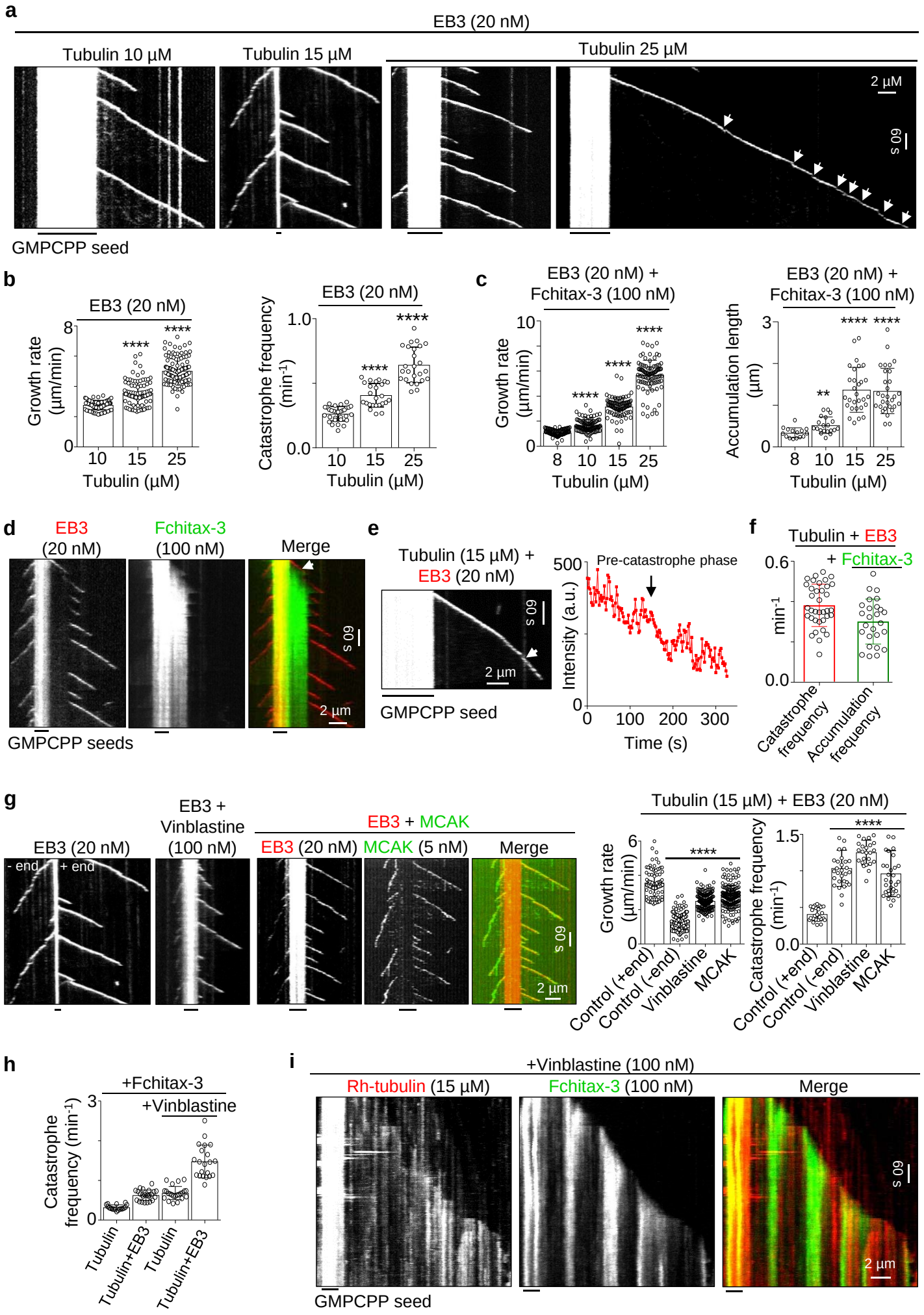

Supplementary Figure 4: Control of the formation of Fchitax-3 accumulations by microtubule dynamics.

a) Representative kymographs (from 3 independent experiments) illustrating microtubule growth from GMPCPP stabilized microtubule seeds in the presence of increasing tubulin concentrations (10 to 25µM) and mCherry-EB3 (20nM). White arrows indicate events of perturbed microtubule growth at higher tubulin concentration.

b) Quantification (mean values) of microtubule growth rates (left panel) and catastrophe frequencies (right panel) in the presence of 10, 15 and 25µM tubulin. n = 80, 92 and 124 growth events from 31, 25 and 25 microtubules for 10, 15 and 25µM tubulin, respectively. Catastrophe frequencies were quantified as an inverted average growth time per microtubule. Error bars represent SD, N=3 independent experiments. ****p <0.0001, Mann–Whitney U-test.

c) Quantification (mean values) of microtubule growth rates (left panel) and the lengths of Fchitax-3 accumulations (right panel) in the presence of different concentrations of tubulin with mCherry-EB3 (20nM) and Fchitax-3 (100nM). n = 105, 101, 90 and 94 for growth rates and n = 16, 21, 30 and 31 for the length of Fchitax-3 accumulations for 8, 10, 15 and 25µM of tubulin, respectively. Error bars represent SD, N=3 independent experiments, **p <0.003, ****p <0.0001, Mann–Whitney U-test.

d) Representative kymographs (from 5 independent experiments) illustrating the occurrence of Fchitax-3 accumulation close to the GMPCPP-stabilized seed (white arrow in the merged panel). The assay was performed in the presence of 15µM tubulin, 20nM mCherry-EB3 and 100nM Fchitax-3.

e) Representative kymographs (from 5 independent experiments) and the respective intensity profile depicting the reduction in the EB3 signal (white arrow in the kymograph) before the onset of a catastrophe.

f) Quantification (mean values) of microtubule plus end catastrophe frequency (n=36) for control microtubules (15µM tubulin, 20nM EB3) and the frequency of Fchitax-3 accumulations at the plus ends (n=26) in the presence of 100nM Fchitax-3 with 15µM tubulin and 20nM mCherry-EB3. For comparing the accumulation frequency with catastrophe frequency, both types of events were analysed as a total number of events observed per unit of time per microtubule. Error bars represent SD.

g) Representative kymographs showing microtubule dynamics in control conditions (15µM tubulin, 20nM mCherry-EB3) or in the presence of 100nM vinblastine or 5nM GFP-MCAK. Bar graphs (mean values) show the quantification of microtubule growth rates (left panel) and catastrophe frequencies (right panel), n = 92, 225, 163 and 175 for growth rates and n = 25, 25, 30 and 32 for catastrophe frequencies for control microtubule plus end dynamics, minus end dynamics, or the plus end dynamics in the presence vinblastine or MCAK, respectively. Catastrophe frequencies were quantified as an inverted average growth time per microtubule. Error bars represent SD, N=3 independent experiments, ****p <0.0001, Mann–Whitney U-test.

h) Catastrophe frequencies per microtubule (mean value) in the presence of tubulin (15µM) and Fchitax-3 (100nM) without (n=18) or with EB3 (20nM, n=24) and without (n=23) or with vinblastine (100nM, n=21). Catastrophe frequencies were quantified as an inverted average growth time per microtubule. Error bars represent SD, N = 3 independent experiments.

i) Representative kymographs (from 3 independent experiments) illustrating microtubule dynamics in the presence of 15µM tubulin supplemented with 3% of rhodamine tubulin in the presence of 100nM Fchitax-3 and 100nM vinblastine.

Supplementary Figure 5

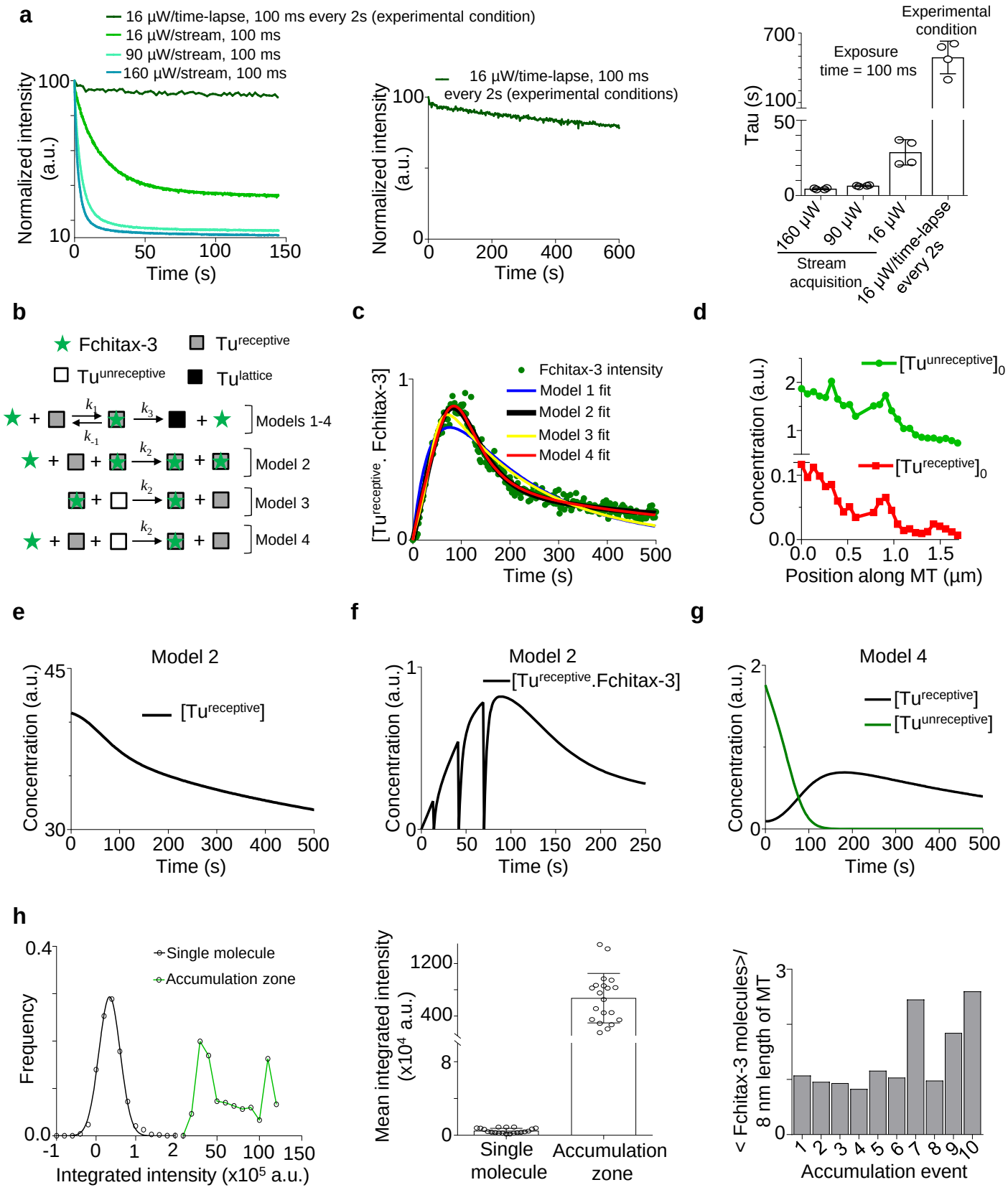

Supplementary Figure 5: Analysis of the kinetics of Fchitax-3 accumulation.

a) Left and middle panel: Characteristic photobleaching traces of Fchitax-3 under different imaging conditions. Fchitax-3 immobilized on a coverslip was exposed to low laser power (10% of maximum laser power, 16μW, 491nm laser line, with a 100ms exposure time, time-lapse acquisition every 2s), used for imaging shown in all our experiments, or with 100ms/stream acquisition with the laser power of 16, 90 and 160 (100% laser power) μW. Curves were fitted with one-phase exponential decay. Right panel: Characteristic decay time (tau) for different conditions measured from one-phase exponential decay was plotted (mean values). N=4 independent experiments, error bars represent SD. When images were acquired using 10% of maximum laser power (16μW, 491nm laser) with 100ms exposure and the interval of 2s (our experimental conditions), Fchitax-3 intensity profile showed 22±8% reduction over 600s, whereas we observe ~60% loss of Fchitax-3 signal within 200s (see Fig. 4a). In our experimental conditions, the characteristic time of Fchitax-3 desorption (corresponding to inverse of rate constant k_3) $\tau_{desorption}$ ~100s is five time faster than the characteristic time of photobleaching, τ_{bleach} ~500s.

b) Schematic kinetic diagrams of the models used (see Methods for details).

c) Comparison of the best fits to a single profile for the considered models.

d) Dependence of initial values [$Tu^{receptive}$] and [$Tu^{unreceptive}$] tubulin states (Model 4) on the position along Fchitax-3 accumulation shown at Fig. 4a,c.

e) Kinetics of [$Tu^{receptive}$] tubulin state from Model 2 shown for profile in (c).

f) Numerically solved FRAP curve generated from Model 2 fit shown in (c).

g) Kinetics of [$Tu^{receptive}$] and [$Tu^{unreceptive}$] tubulin states from Model 4 shown for profile in (c). The plots (c-g) represent numerical solution of analytical equations with parameters taken from best fits to experimental curve shown in Fig. 4c.

h) Histograms of fluorescence intensities (left panel) and mean integrated intensities (mean values, middle panel) of Fchitax-3 bound to coverslip during the reaction and Fchitax-3 at accumulation zones. Error bars represent SD, n=20, N=5 independent experiments. Right panel: analysis of the number of Fchitax-3 molecules in the regions of strong Fchitax-3 accumulation for 10 different microtubules.

Supplementary Figure 6

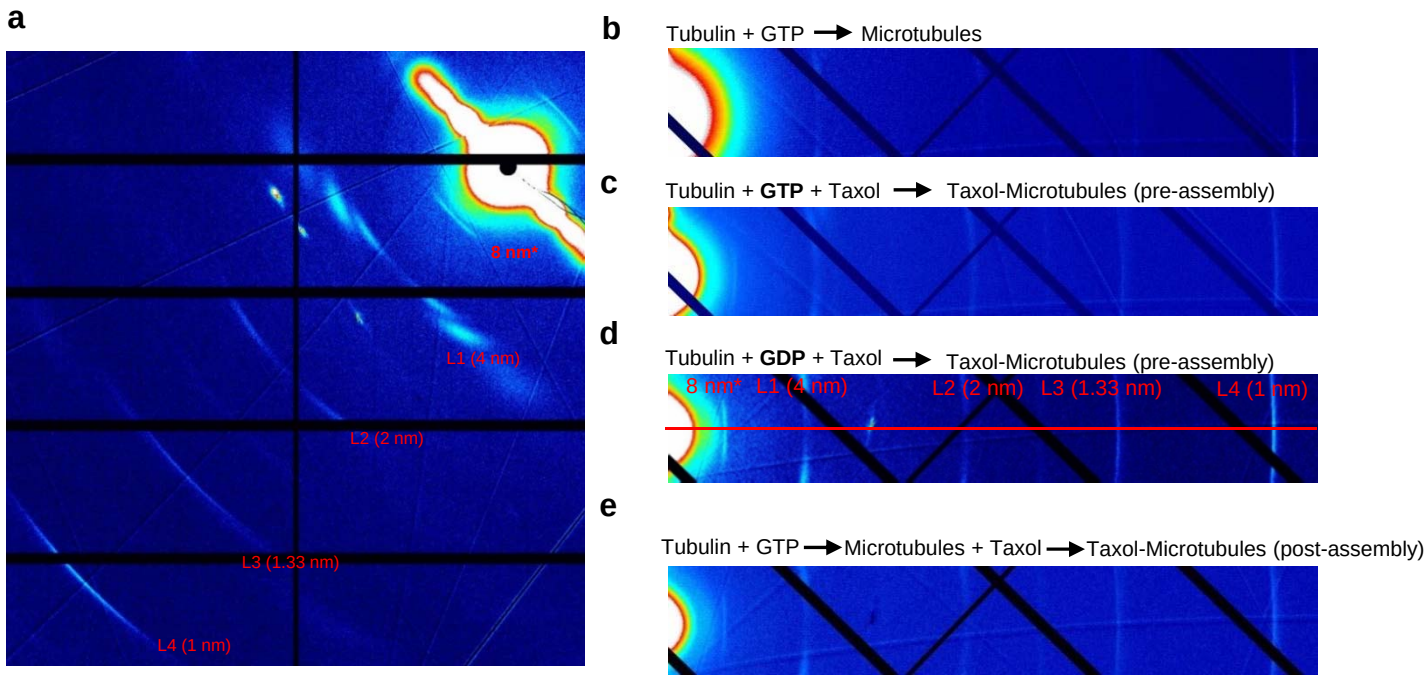

f

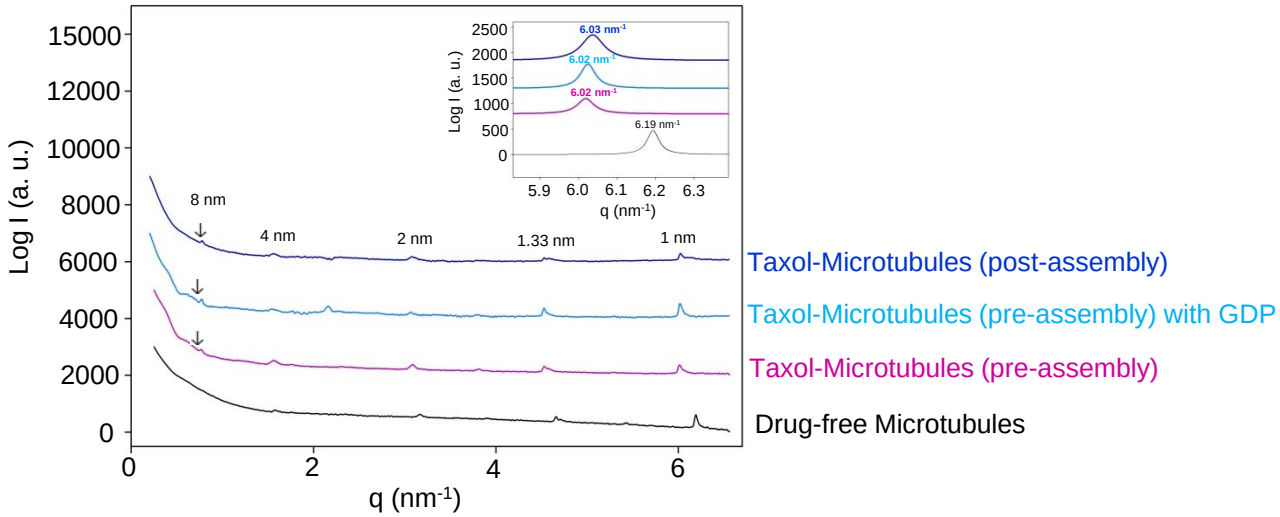

g

Microtubule samples	Drug-free Microtubules	Taxol-microtubules Pre-assembly	Taxol-microtubules Pre-assembly (with GDP)	Taxol-microtubules Post-assembly
Avg. monomer length (nm)	4.06 ± 0.01	4.18 ± 0.01	4.18 ± 0.01	4.16 ± 0.01
Avg. dimer length (nm)	8.12 ± 0.02	8.35 ± 0.02	8.35 ± 0.02	8.32 ± 0.02
1 nm peak position (nm^{-1})	6.19 ± 0.01	6.02 ± 0.01	6.02 ± 0.01	6.03 ± 0.01

Supplementary Figure 6: X-ray fiber diffraction of microtubules in the presence of taxol in different assembly conditions.

a) Averaged and background subtracted microtubule diffraction image (example from microtubules assembled from GDP tubulin in the presence of Taxol, 4 independent experiments).

b-f) Meridional planes of drug-free microtubules assembled from GTP-tubulin (black line in f), microtubules assembled from GTP-tubulin in the presence of Taxol (pre-assembly conditions, purple line in f) or GDP-tubulin in the presence of Taxol (blue line in f), and microtubules assembled from GTP-tubulin in the absence of Taxol and treated with Taxol after assembly (post-assembly conditions, deep blue line in f). The red line in d shows the line considered for plotting the intensities in qx space. Panel f shows Meridional intensity patterns, with the inset illustrating the best fit of 1nm band experimental intensities to a Lorentzian distribution. Images are representative of 4 independent experiments.

g) Fiber diffraction analysis of microtubules during different assembly conditions in the presence of Taxol. All Taxol-treated samples showed an 8 nm layer line, indicating a difference between α- and β-tubulin axial spacing and thus demonstrating that the observed dimer rise is due to differential monomer expansion. Data represent mean ± SEM. n=24, N=4 independent experiments.

Supplementary Figure 7

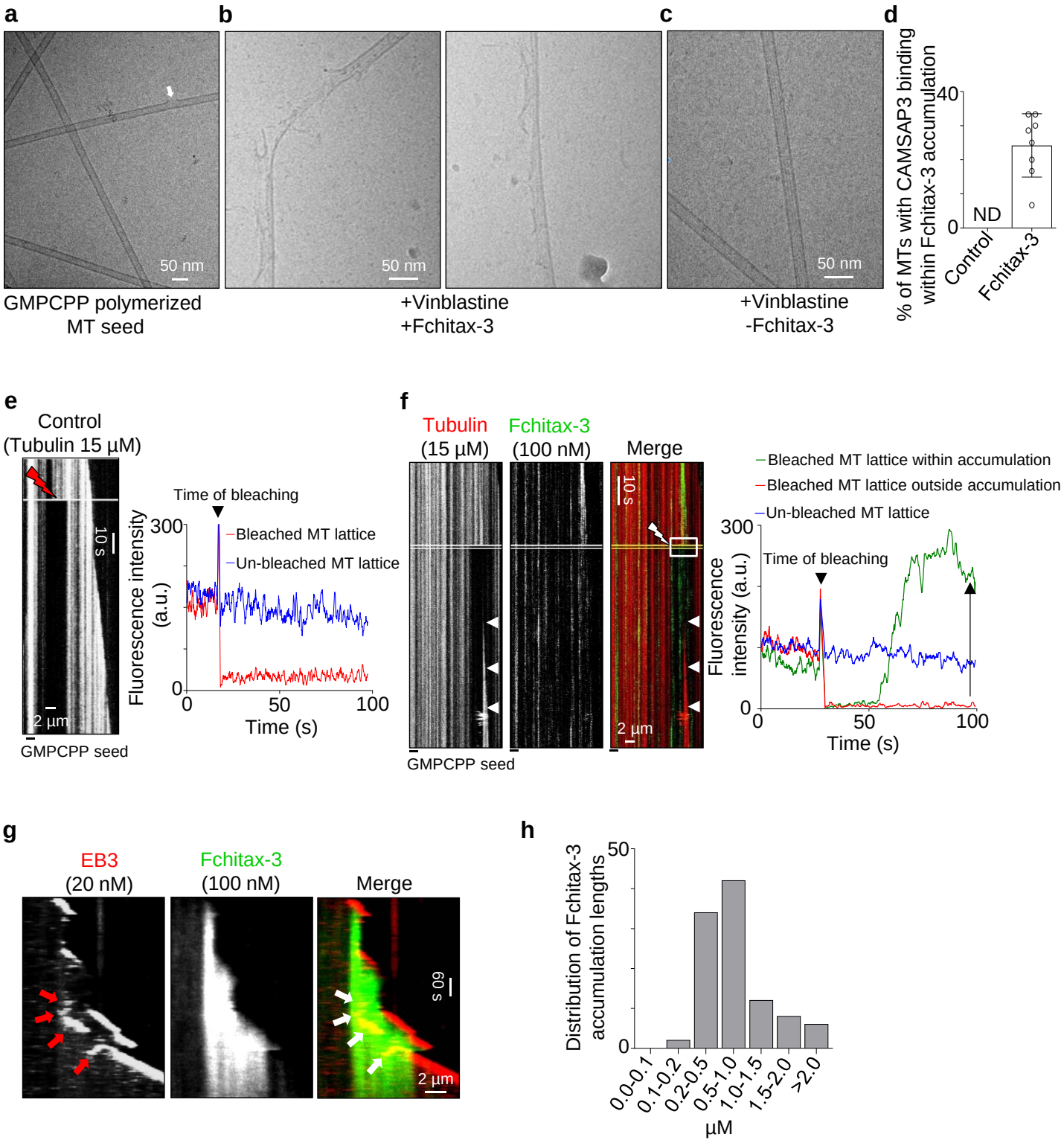

Supplementary Figure 7: Analysis of Cryo-EM data and FRAP experiments.

a-c) Representative Cryo-EM images (N = 2 independent experiments) illustrating the structure of GMPCPP-stabilized microtubule seeds (a), microtubules grown from GMPCPP-stabilized microtubule seeds in the presence of 15µM tubulin, 20nM EB3 and 100nM vinblastine with (b) or without (c) 100nM Fchitax-3. White arrow shows the presence of a very small defect within GMPCPP-stabilized microtubule seeds. Scale bars, 50nm.

d) Quantification (mean value) of percentage of Fchitax-3 accumulation found to be positive for CAMSAP3 binding. Error bars represent SD, n=27 accumulation events in 7 independent experiments, ND = not determined, as no such events were observed.

e) A representative kymograph (left panel, N = 3 independent experiments) and fluorescence intensity profile (right panel) showing fluorescence recovery after photobleaching in a control microtubule (15µM tubulin supplemented with 3% rhodamine tubulin). The bleached microtubule region is highlighted by a red lightning bolt.

f) Left panel: representative kymographs (N = 3 independent experiments) showing fluorescence recovery after photobleaching within microtubule lattice associated with Fchitax-3 accumulation (15µM tubulin supplemented with 3% rhodamine tubulin, 100nM Fchitax-3). The bleached microtubule region is highlighted by a white lightning bolt, and bleached microtubule area is shown by a white box. Robust tubulin incorporation within the bleached microtubule lattice associated with the Fchitax-3 accumulation zone is highlighted by white arrowheads. Right panel: fluorescence intensity profiles of an unbleached and a bleached microtubule region with and without Fchitax-3 accumulation. Strong recovery of fluorescence after bleaching within Fchitax-3 accumulation region is highlighted by a red arrow.

g) Representative kymographs (N = 5 independent experiments) showing transient EB3 binding (highlighted by red arrow in EB3 panel and white arrow in merged panel) within the Fchitax-3

accumulation area. The experiment was performed in the presence of tubulin (15µM), mCherry-EB3 (20nM) and Fchitax-3 (100nM).

h) Distribution of the Fchitax-3 accumulation lengths observed in vitro. n=104 accumulation events from 7 experiments.

Supplementary Video 1. Fchitax-3 accumulation at the growing microtubule plus end.

The movie illustrates formation of an Fchitax-3 accumulation close to the growing microtubule plus end, as depicted in Fig. 2a. The experiment was performed in the presence of tubulin (15 µM), mCherry-EB3 (20 nM) and Fchitax-3 (100 nM). The movie consists of 177 frames acquired with a 2s interval between frames and an exposure time of 100ms. Scale bar, 2µm. The movie is representative of more than 5 independent experiments.

Supplementary Video 2. Laser severing experiment showing Fchitax-3 accumulation zone stabilizes microtubule lattice.

The movie starts just after ablating the Fchitax-3 accumulation area with a 532nm laser as shown in Fig. 2h. After ablation of the growing microtubule at Fchitax-3 accumulation, both the newly generated ends survived and started growing again. The experiment was performed in the presence of tubulin (15µM, supplemented with 3% rhodamine-tubulin), mCherry-EB3 (20nM) and Fchitax-3 (100nM). The movie consists of 750 frames acquired in a stream acquisition mode with an exposure time of 100ms. Scale bar, 2µm. The movie is representative of 5 independent experiments.